Measurements of silicon photomultipliers at different operating points and simulation with GEANT4

submitted by
Andreas Künsken

Master's Thesis in Physics

presented to

Faculty of Mathematics, Computer Science and Natural Sciences

at RWTH Aachen University

November 2012

made at

III. Physics Institute A

Univ.-Prof. Dr. Thomas Hebbeker

Abstract

A temperature regulation and stabilization system for silicon photomultipliers is designed, tested and integrated into an optical test stand. A set of operating parameters of different silicon photomultipliers at various temperatures is obtained by measurement. These parameters are the pulse shape of the signal, the thermal noise rate, the crosstalk probability and the afterpulsing probability. For detector simulations a dedicated silicon photomultiplier simulation model in GEANT4 is extended and adapted. This model is then fed with the previously obtained parameters. Subsequently, the functionality of the model is validated by means of performing the same analysis on the simulation output as before on the measured data. The model proves itself to be capable of simulating all basic features of a silicon photomultiplier.

Zusammenfassung

In dieser Arbeit wird ein Temperaturregulations- und -stabilisationssystem für Silizium-Sekundärelektronenvervielfacher entworfen, getestet und in einen optischen Teststand integriert. Bei verschiedenen Temperaturen werden dann die Betriebsparameter verschiedener Silizium-Sekundärelektronenvervielfacher durch Messungen bestimmt. Diese Parameter sind die Pulsform des Signals, die thermische Rauschrate, die optische Übersprechwahrscheinlichkeit und die Nachpulswahrscheinlichkeit. Anschließend wird ein spezielles Silizium-Sekundärelektronenvervielfachersimulationsmodell für Detektorsimulationen erweitert und angepasst und mit den vorher bestimmten Parametern betrieben. Danach wird die Funktionalität des Modells durch Anwenden der gleichen Analysen auf die simulierten Daten wie auf die Messdaten verifiziert. Das Simulationsmodell erweist sich als fähig die essenziellen Eigenschaften eines Silizium-Sekundärelektronenvervielfachers zu simulieren.

Contents

List of Figures

List of Tables

1 Introduction

A wide range of experiments depends on the ability to detect light efficiently and reliably. For a long time, photomultiplier tubes (PMTs) that consist of a photo cathode and a set of dynodes served this purpose well. Yet, PMTs require an operating voltage of some kV and often occupy a lot of space (see Fig. 1.1). This hampers

Figure 1.1: Image for comparison of the different sizes of a PMT (left) next to an SiPM (right). Taken from [1].

the construction of a compact detector system. With the discovery of the photon-triggered electron-hole-pair creation in solids, which is not to be confused with the e^+-e^--pair production, a new and promising possibility to build photon detectors was found. The rather simple detector principle is a diode which is operated with a direct current voltage in reverse direction. On electron-hole-pair creation, the charge carriers are being pulled out of the diode by the applied voltage and because of avalanche charge multiplication a measurable voltage pulse is generated. The development of these avalanche photo diodes started with basic p-n-junctions in reverse bias that give a current which is proportional to the incident light flux. By the time the diodes were specialized and it became possible that a single photon may trigger an avalanche. The latest products consist of several of these single photon avalanche diodes as pixels and are capable of a linear response to the photon number for not too large amounts of light. These multi-pixel photon detectors are often made of silicon and, therefore, are called silicon photomultipiers (SiPMs). SiPMs present

themselves with a multitude of positive features. In this context the operating voltages of about 30 V to 70 V, which are significantly lower compared to PMTs, have to be mentioned along with the smaller device size of some millimeters. However, SiPMs also show some disadvantages, for example the device size dependent dark noise that may add up to several Megahertz of dark count rate and, additionally, is strongly temperature dependent. This can be seen in Fig. 1.2, where the noise rate of an SiPM is shown depending on the pulse height for different temperatures. Besides that there are further noise effects, afterpulsing and optical crosstalk, which

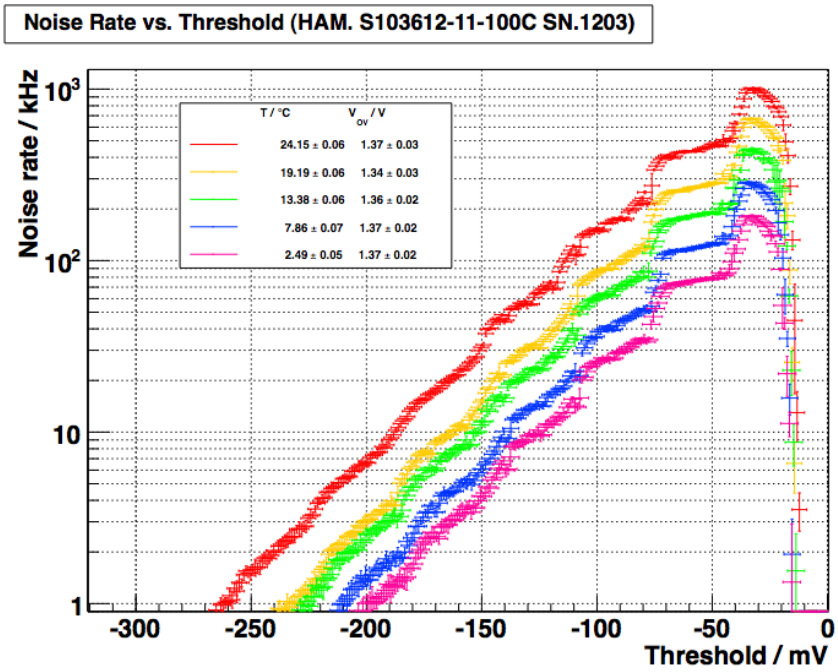

Figure 1.2: Noise rate of an SiPM over threshold voltage for the trigger. The different colors are for different temperatures where red is the warmest and pink the coldest operating temperature. Taken from [2].

are as well depending on the operating temperature of the SiPM and lead to an overestimation of the detected photon count. Due to the fact that SiPMs are already wide-spread in a lot of experimental and practical applications as for example in the CMS[1] detector at the LHC[2] or PET[3] in medical physics it is even more crucial to be able to characterize the noise including its temperature dependence and to create realistic SiPM simulations. This may help understanding a detector's performance before its commissioning. In the course of this thesis an extension to an already existing test stand for SiPM characterization is built which is used to manipulate

[1] **C**ompact **M**uon **S**olenoid
[2] **L**arge **H**adron **C**ollider
[3] **P**ositron-**E**mission-**T**omography

and monitor the SiPM's operating temperature. The noise components are analyzed regarding their temperature dependence and the gained information is implemented into an existing SiPM simulation which is capable of reproducing the results of the measurements.

2 Silicon Photomultipliers

In order to understand the behavior of silicon photomultipliers (SiPMs) it is inevitable to take a look at the working principle of semiconductors in general. Therefore, in the first part of this chapter a short introduction into semiconductor physics and semiconductor photon detection is given. Afterwards, in the second part of the chapter, the properties of SiPMs are studied.

2.1 Semiconductors

2.1.1 p-n Junctions

For comprehending the conductive properties of a material it is necessary to look at the valence band and the conduction band of the material. The energy distance between the valence band and the conduction band determines whether the material is to be considered a conductor, a semiconductor or an insulator (cf. Fig. 2.1). When the conduction band and the valence band overlap, electrons can enter the conduction band without requiring additional energy because the Fermi level E_F lies higher than the lower bound of the conduction band. In contrast to that an insulator has a gap between the valence band and the conduction band and the Fermi level lies in between them. This gap is called the band gap. Because of the band gap the electrons cannot get into the conduction band without extra energy and the material does not conduct currents. For semiconductors the band gap has a width of up to three electron volts (eV) which for itself would also not support a good conduction performance. Yet it is possible to increase the conductivity. For silicon, which is the mainly used material for SiPMs, this is done by doping. Although the band gap of silicon is with 1.12 eV larger than the smallest possible band gaps of less than 1 eV (see [4]), it is easier to handle and relatively inexpensive. By doping silicon, additional energy levels in the band gap are introduced close to the valence band (p-doping) and the conduction band (n-doping), accordingly, which are on the order of 50 meV (c.f. [5]). When bringing n-doped and p-doped material together the electrons and holes recombine within a certain range of the junction and create a space charge region, often called depletion zone. This device is called a diode where the n-doped area is called cathode and the p-doped area anode. As the Fermi levels of p-doped and n-doped material are initially different but align at the junction, a built-in potential develops between the two parts of the diode. It now depends on the polarity of an applied voltage whether the diode conducts a current or inhibits it. In the case of a positive pole on the anode and a negative pole on the cathode the diode conducts the current after overcoming the built-in potential which eliminates the space charge region. This way of biasing the diode is called forward bias whereas

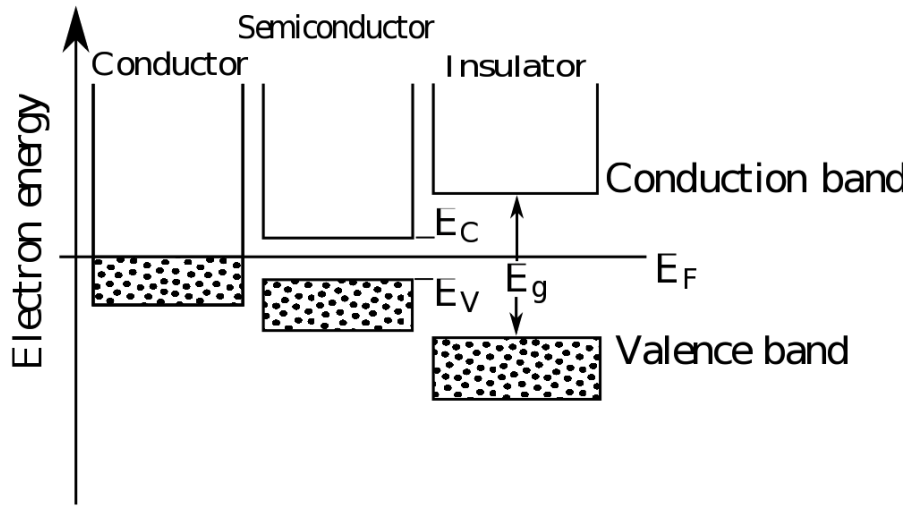

Figure 2.1: Different energy levels in relation to Fermi Energy E_F from left to right for a conductor, a semiconductor, and an insulator. Adapted from [3].

the opposite polarity is the reverse bias which widens the space charge region and keeps the diode from conducting currents. The latter effect is being used when operating SiPMs because then the diode only conducts a current when a free charge carrier pair was created inside the depletion zone.
There are several ways of creating a pair of free charge carriers inside the depletion zone. Two ways are depicted in Fig. 2.2. The first way is by overcoming the small barrier between the extra levels that are introduced with doping and either the conduction band or the valence band via thermal excitation. This is possible by gaining the necessary energy out of the crystal lattice oscillations in the silicon and is shown by the vertical transition.
The second method is tunneling through the barrier. This may occur under strong reverse bias where the bending of the bands at the interface between the n-doped and p-doped areas in the silicon gets very steep. The horizontal transition in Fig. 2.2 illustrates the tunneling process.
A third way is the crossing of the small gap between an extra level and the bands by absorbing a photon. If the applied bias voltage is large enough to achieve a multiplication of the initial electron-hole pair by creating further electron-hole charge carrier pairs on collision of a charge carrier with an atom, the detection of photons gets possible. The process of charge multiplication is also known as avalanche multiplication or for short as an avalanche. Diodes working in this way are called avalanche photo diodes (APDs) and produce an output signal that is proportional to the amount of light that hits the detector. With further increase of the bias voltage also the holes gain enough energy to create new charge carriers. In Fig. 2.2(b) one may see that when the holes also start multiplication, there are again electrons lifted into the conduction band at the border of the junction that start new multiplication processes

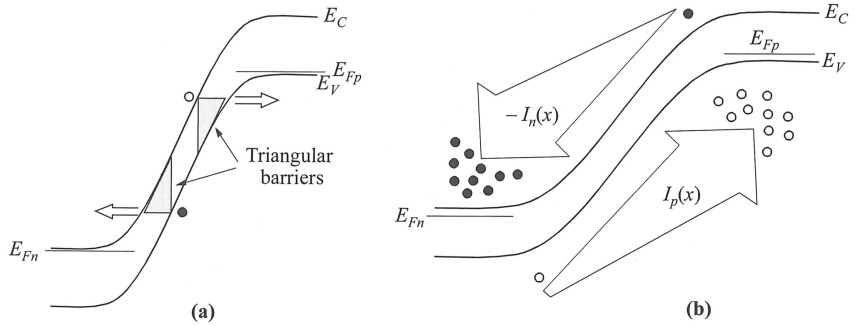

Figure 2.2: Demonstration of gap crossing and multiplication in a p-n-junction. (a) Via tunneling it is possible to cross the barrier horizontally, if the bending of the bands gets steep enough. A vertical transition could be achieved e.g. by thermal excitation. (b) Avalanche multiplication process in the band scheme for electrons (filled circles) and holes (open circles). Image adapted from [6].

themselves. The threshold voltage needed is called the breakdown voltage. At this time the avalanche is self sustaining and the avalanche will not stop by itself. In this setup a single photon may trigger the breakdown similar to a Geiger-Mueller-counter where a single particle interaction triggers the counter. Due to this similarity an APD operated this way is referred to as a geiger-mode APD (GAPD). Because of the fact that an avalanche in a GAPD will not stop on its own it is necessary to quench the developing current in the GAPD or it will blow and be destroyed. The current is quenched by the means of either passive quenching with a resistor or active quenching where a circuit briefly switches off the supply of the diode. The GAPD together with its quenching circuit is what constitutes a pixel in an SiPM.
In SiPMs usually the passive quenching is used and works as follows. During breakdown the diode gets conductive because of the avalanche and the diode resistance compared to the quenching resistor gets negligible. Thus the major part of the bias voltage now drops across the quenching resistor and the diode voltage drops below breakdown voltage. Now only electrons contribute to the multiplication which inhibits the self-sustaining avalanche and finally all charge carriers are drawn out of the diode volume. Then the diode is non-conductive again and the diode voltage rises, restoring the initial diode state. During quenching the GAPD is not capable of detecting further photons and the time to recover the diode's operational state is hence called recovery time. The recovery time for GAPD cells in on the order of magnitude of 30 ns (c.f. e.g. [7]).

2.1.2 GAPD Structure

The probability of an interaction of photons with the GAPD and the distance photons travel in the silicon depend on the wavelength of the incoming photon as well as the

material of the GAPD itself. Fig. 2.3 shows the absorption coefficient of Si and GaAs in dependence of the energy of the incoming photon. Assuming a photon

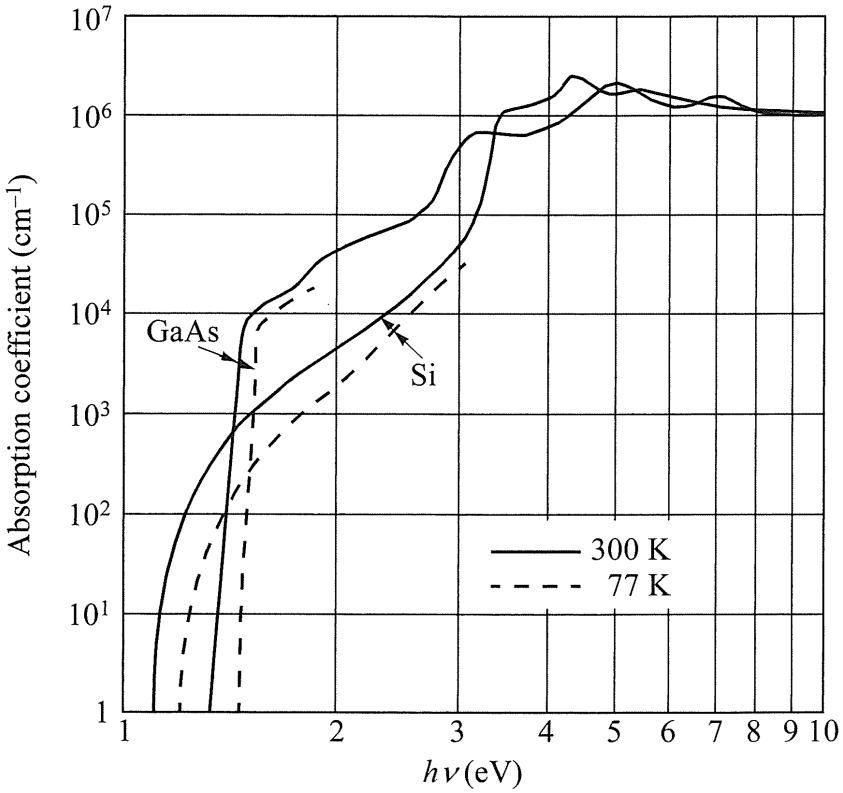

Figure 2.3: Absorption coefficient for Si and GaAs over the energy of the incoming photon. For an 400 nm photon wavelength ($\approx$ 3.1 eV) silicon absorbs already about 10 photons per µm. Image from [6].

with a wavelength of 400 nm, which is approximately the wavelength of scintillation light in a number of experiments, one may calculate the number of photons that are absorbed on the average when light of this wavelength passes silicon. It becomes obvious that for low light levels in the expected wavelength regime basically all light is being absorbed within the first micrometers of a GAPD while it is becoming more and more transparent for longer wavelengths.
Furthermore, the probability to trigger an avalanche in a p-n-junction depends on the doping type of the material as well as whether electrons or holes are the charge carriers that are accelerated to initiate an avalanche (see Fig. 2.4). One may see that electrons are triggering more homogeneously once they have penetrated far enough into the silicon. This is not the case for holes. Moreover, electrons have a per se higher triggering probability than holes.
Thus, it is advantageous to adapt the GAPD structure to the expected wavelength of the photons that need to be detected and to support electron induced triggering

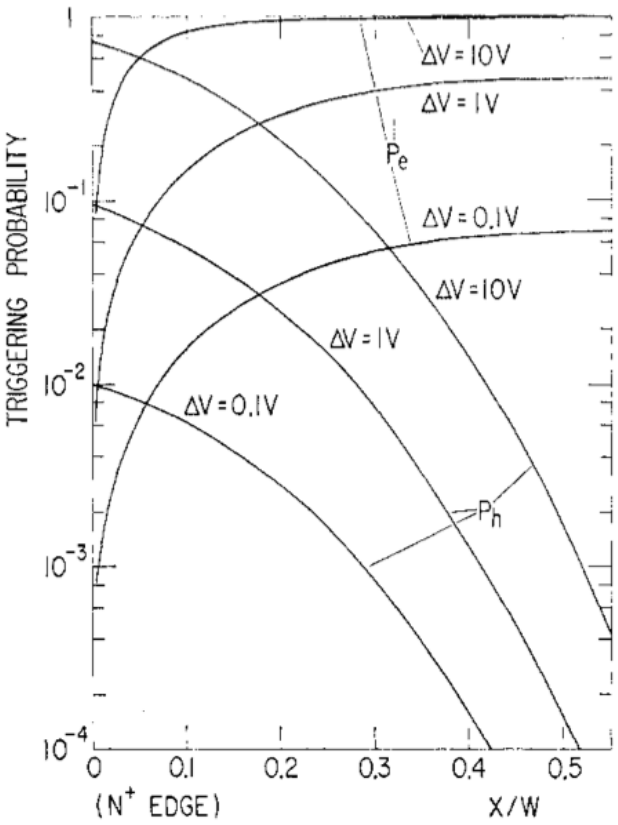

Figure 2.4: Avalanche trigger probability for electrons (P_e) and holes (P_h) vs. depth in a reverse biased diode for different ΔV, which is the difference between applied voltage and breakdown voltage. The abscissa is given in units of fraction of the depth x over the whole device depth. Image taken from [8].

in order to maximize the efficiency in photon detection. A typical SiPM cell ([9]) that is sensitive to blue light is shown in Fig. 2.5 and consists of an n-type carrier substrate on which lies another n-type epitaxial layer but with lighter doping density. The second layer is there for handling purposes and separation of cells. Afterwards a highly doped n layer is attached onto the epitaxial layer followed by a highly p-doped layer. These two form the multiplication area. On top of the p layer there is a shallow layer of even higher doped p material. This is for ensuring a homogenous field configuration in the cell which is necessary for a homogenous charge multiplication over the whole cell area. The thickness of the cell from the beginning of the epitaxial layer to the top is on the order of 2 µm to 4 µm and the p layers together have a thickness of approximately 0.5 µm (c.f. [9]). The overall thickness of an SiPM cell depends on the thickness of the silicon wafer that was used but is usually in the range of 300 µm to 600 µm.

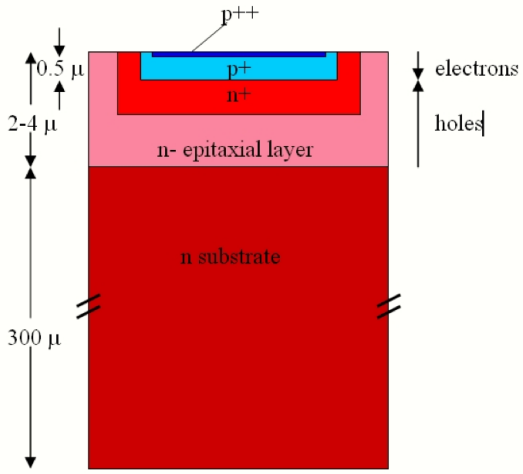

Figure 2.5: Architecture of an SiPM cell. The p on n structure is sensitive to blue light. Image from [9].

2.2 Silicon Photomultipliers

Having explained the basic working principle of a single SiPM cell with respect to semiconductor physics it is now possibile to describe the complete SiPM as an array of GAPDs. In this section, the SiPM's properties in detecting photons and its noise source in measurements are studied. When talking about the SiPM response it is important to know that the SiPM gives only an output of voltage pulses of a certain height which is shown in Fig. 2.6. On the one hand this height depends on the number of cells that triggered and on the other hand of the pixel gain which itself depends on the applied bias voltage. The smallest pulse an SiPM is able to output is referred to as a one photon equivalent (1 p.e.). Larger pulses are integral multiples of these with some uncertainty due to statistical processes in the cell. Another useful quantity that is often used in the context of SiPMs is the overvoltage which is defined as

$$V_{OV} = V_{Bias} - V_{BD} \tag{2.1}$$

where V_{Bias} denotes the applied bias voltage and V_{BD} is the breakdown voltage above which the cell enters geiger-mode. The overvoltage is about some volts and has an influence on the pixel gain and the detection efficiency of the SiPM as well as the noise rate.

2.2.1 Photon Detection Efficiency

For experiments in which photon counting is performed it is important to know how efficiently an SiPM detects single photons. For this purpose the photon detection efficiency (PDE) is defined as

$$PDE = FF \times QE \times P_{Trig}, \tag{2.2}$$

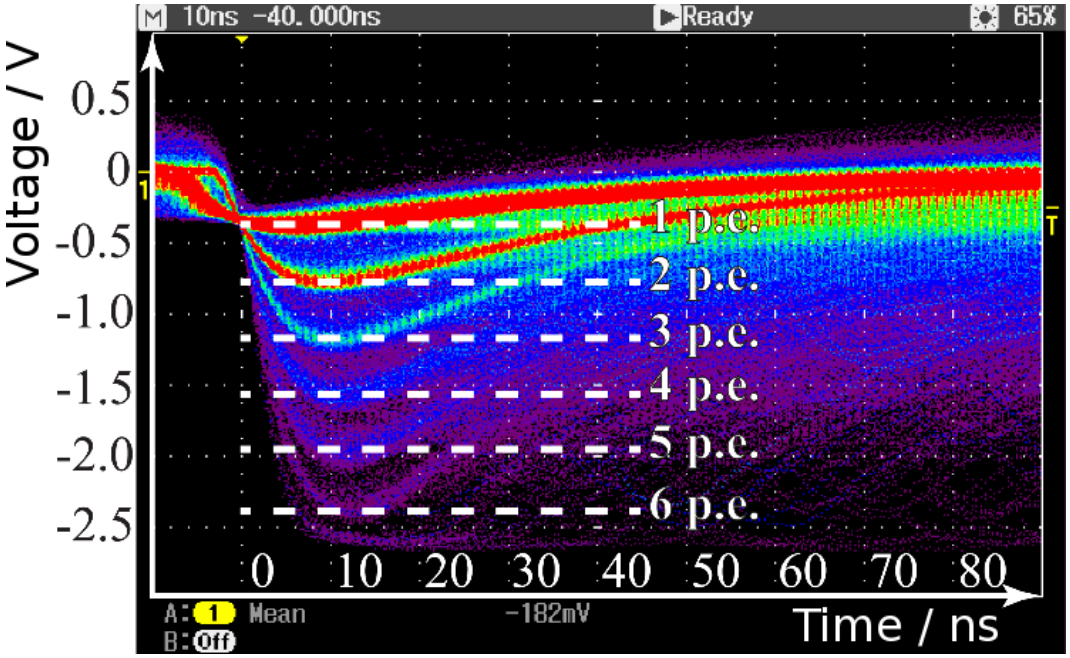

Figure 2.6: Voltage traces of an SiPM in the dark. Clearly visible are the discrete pulse heights that are multiples of the 1 p.e. amplitude. Adapted from [1].

with FF being the fill factor, QE being the quantum efficiency, and P_{Trig} denoting the avalanche triggering probability.
In equation 2.2 the fill factor respects the geometrical dimensions of the SiPM as the circuits needed to quench the avalanche in geiger mode require some space and cannot be used for detecting photons. Thus the fill factor is the ratio of active area to whole area. With shrinking pixel size the fill factor decreases as well (c.f. Fig. 2.7). This is because of the space required for the quenching circuits does not get smaller in the same way the pixel area does. Additionally, some space is required for the connecting grid of the pixels. Typical values for fill factors are from ≈ 30 % for 25 µm pixel pitch to ≈ 80 % for 100 µm pixels (c. f. [11], [12], [13]).
QE denotes the quantum efficiency, which is the wavelength-dependent probability for a photon to create an electron-hole pair. Finally, the trigger probability (P_{Trig}) takes into account that not every charge carrier pair causes an avalanche and is thus calculated as the ratio of triggered avalanches and created primary electron hole pairs. Fig. 2.4 shows the behavior of P_{Trig} in relation to V_{OV} for electrons and holes. The fast rise and the early saturation of the comparably high triggering probability for electrons underlines that electron triggered avalanche devices are most promising for fast and efficient applications. It is evident that P_{Trig} depends both on V_{OV} and the temperature. Fig. 2.8 shows a typical detection efficiency spectrum for an SiPM used in the scope of this thesis. With these considerations regarding eq. 2.2 it is

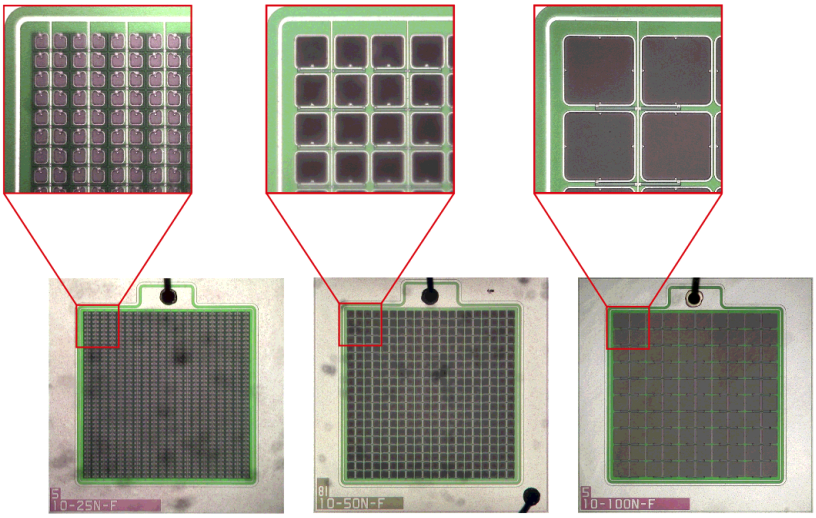

Figure 2.7: Magnified view of pixels in an SiPM. The black squares are the active area whereas the green spaces in between the cells are needed for quenching resistors and separation of the cells and cannot detect photons. Taken from [10].

obvious that the PDE is a strongly depending function of the operating parameters, and for measurements of low light levels it is inevitable to know the behavior of it to avoid miscalculation of the incoming photon flux. However, another important quantity influencing the PDE is the incoming photon flux itself. That is because for high photon fluxes the recovery time of the pixels is not negligible in comparison to the mean time distance between two pixel hits and the SiPM response saturates. A linear response of the SiPM is only possible if for a time window on the order of the recovery time of a cell the condition

$$\mathrm{N}_\gamma \ll \mathrm{N}_{\mathrm{pix}} \tag{2.3}$$

holds. In Fig. 2.9 the SiPM saturation for the number of fired pixels is shown for three different pixel numbers. It is obvious that devices with a larger pixel count are capable of a linear response in a wider range than devices with smaller pixel counts are. In general, the development of the number of fired pixels in dependence on the number of incident photons may be calculated for a specific device via

$$N_{fired} \approx N_{pixel} \cdot \left(1 - e^{-\frac{N_{Photon} \cdot PDE}{N_{pixel}}}\right) \tag{2.4}$$

as was found in [9].

2.2.2 Noise in SiPMs

In addition to the possibility that a photon which hits an SiPM pixel is not detected a pixel may as well output a signal when there is no light. This is referred to as

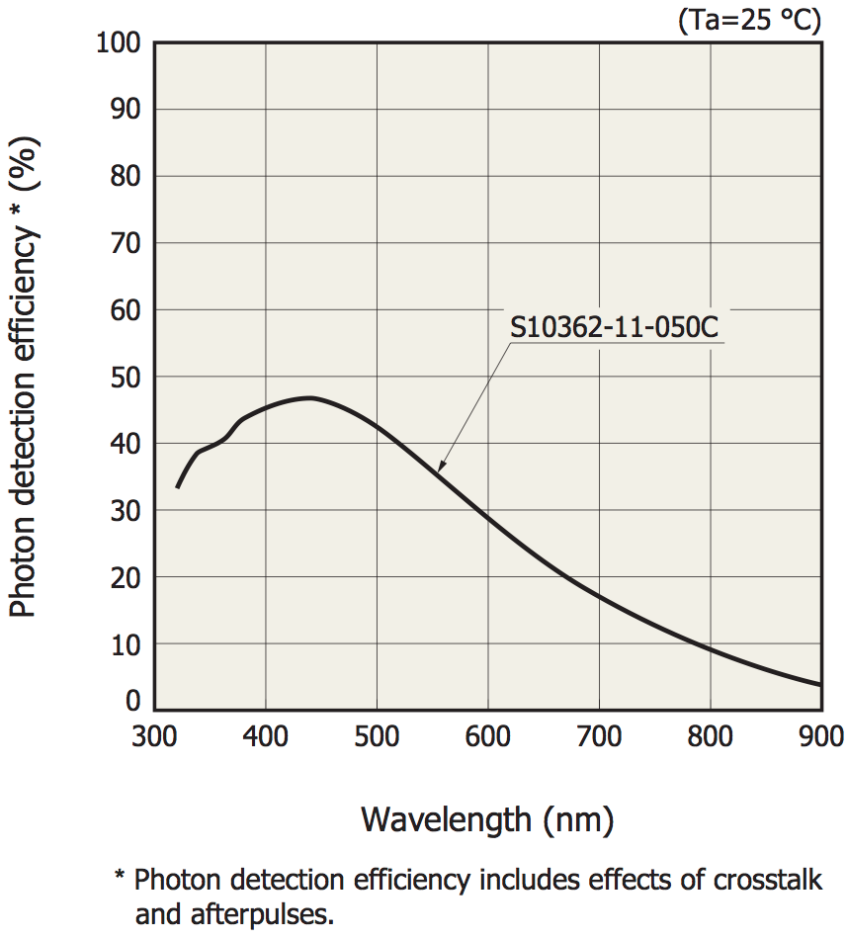

Figure 2.8: Photon detection efficiency spectrum of a 1×1 mm^2 SiPM. The peak sensitivity lies at a wavelength of 440 nm. Plot taken from [11].

SiPM noise. One may distinguish the SiPM noise regarding its occurrence between thermal noise, which is always present, and correlated noise coming from afterpulsing and crosstalk. A thorough analysis of the noise is performed in [15], [16] and [17]. The noise, if not treated correctly, may lead to an overestimation of the incident photon flux. However, the SiPM noise, like the PDE, is a strongly depending function of the operating parameters and has different origins which makes it difficult to account for in the analysis.

Thermal Noise

The small energy band gaps on the order of magnitude of 50 meV that develop because of doping (see section 2.1) may not only be crossed by electrons because of photon excitation but also by thermal excitation because of phonons in the crystal

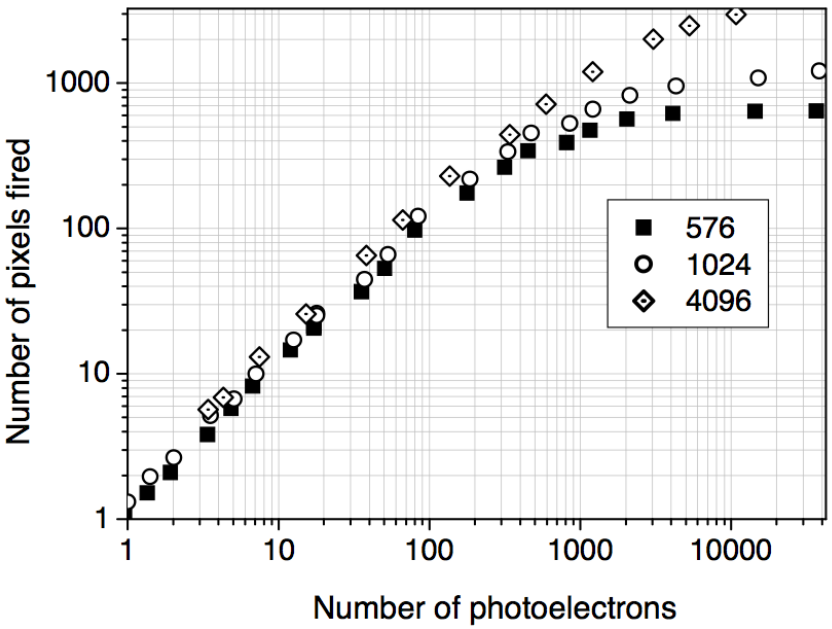

Figure 2.9: Saturation of SiPMs on a high number of created photoelectrons for three different device pixel numbers. Plot from [14].

lattice. A charge carrier pair created by this means in the sensitive volume of the SiPM may trigger an avalanche and the SiPM cell breaks down without light. This type of SiPM noise is always present and leads to a constant offset in photon counting if not properly corrected for. The thermal noise rate of the SiPM increases with the temperature as the phonons are more likely to have enough energy to create a charge carrier pair. A rise of the bias voltage causes an increase of the output amplitude and also the thermal noise rate, as P_{Trig} is rising with the applied voltage as well (see [2]). Table 2.1 shows typical noise rates for two series of SiPMs with different pixel sizes for an output threshold of 0.5 p.e. at 25 °C. An explanation for the increase in the noise rates with increasing pixel sizes is the higher fill factor for the SiPMs. Therefore, a larger volume per area in which thermal noise may occur is given.

Afterpulsing

From impurities in the silicon lattice it is possible that foreign atoms introduce deep energy levels that are capable of trapping charge carriers during an avalanche (see Fig. 2.10). These energy levels are not stable and release the charge carriers with a certain time delay. If this happens when the initial avalanche is over and the cell would in principle be able to detect a photon, the now released charge carrier may again retrigger the cell and cause a second avalanche. In general it is not possible to distinguish whether a pixel fired from afterpulsing or something different. However, it is possible to determine the probability for an afterpulsing event from a statistical

SiPM series	*Hamamatsu S10362-33*			*Hamamatsu S10362-11*			*Ketek* PM3350
Total area	3×3 mm^2			1×1 mm^2			3×3 mm^2
Pixel pitch in µm	100	50	25	100	50	25	50
Pixel number	900	3600	14400	100	400	1600	3600
FF in %	78.5	61.5	30.8	78.5	61.5	30.8	70
Typ. noise rate in MHz	8	6	4	0.6	0.4	0.3	-
Noise per area in MHz/mm^2	0.89	0.67	0.44	0.6	0.4	0.3	≤ 0.5
Max. noise rate in MHz	12	10	8	1	0.8	0.6	≤ 4.5

Table 2.1: Dark noise rates, pixel pitch, fillfactor, and pixel number for different SiPMs as stated in the datasheets [11], [12] and [13]. The Ketek PM3350 is a specific device not a series. Geometrical efficiency stated by Ketek was taken as the SiPM's fill factor.

point of view if the time constant for releasing the charge carrier is not larger than the mean time difference between two thermal noise events ([17]). It was found that there are at least two time constants dominant in an SiPM. A short fraction with a time constant of $\tau_{\mathrm{AP,s}} \approx 10$ ns and a long fraction with a time constant of $\tau_{\mathrm{AP,l}} \approx 100$ ns. [17].

Crosstalk

When operating an SiPM in the dark it is possible to get a response of the device that corresponds to several simultaneously fired pixels. Assuming Poisson statistics it is possible to calculate the probability for two or more thermal noise events to happen at the same time. Thus, for the probability of a certain number of events in a given time window

$$P(k) = \frac{\mu^k}{k!} \cdot e^{-\mu} \tag{2.5}$$

applies, where k is the number of events, e is Euler's number and μ is the average event count calculated by multiplying the noise rate with the time window. For a 3×3 mm^2 SiPM the noise rate is stated by the manufacturer to be around 8 MHz at a 0.5 p.e. threshold (see Table 2.1). The rise time for SiPM pulses is on the order of nanoseconds and, thus, to determine the number of events that happen approximately at the same time the average noise rate in a 10 ns time window should be sufficient to estimate the probability for more than one triggering event at the

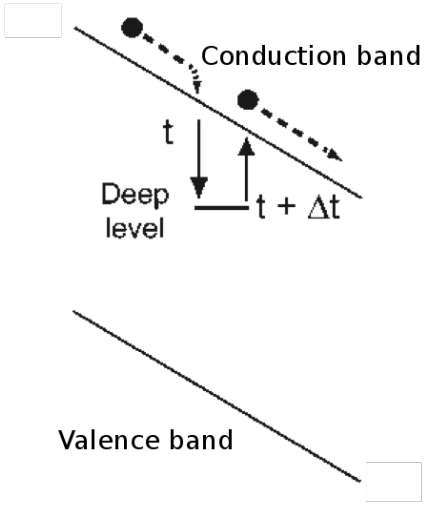

Figure 2.10: Image of the band structure for charge carrier trapping during an avalanche. Image adapted from [18].

same time. With $\mu = 10\ \text{ns} \cdot 8\ \text{MHz} = 0.08$, the probability then calcutes to

$$\begin{aligned} P(N > 2) &= 1 - P(0) - P(1) && (2.6)\\ &= 1 - 0.923 - 0.0738 && (2.7)\\ &= 0.003 && (2.8) \end{aligned}$$

However, events in which several pixels fire at the same time may be observed frequently. As it is very unlikely that these events stem from thermal noise there has to be another reason for them which is optical crosstalk. As is shown in Fig. 2.11 it is possible that during an avalanche there are photons emitted from the cell. These photons may trigger avalanches in adjacent cells by different means. One possible way is the direct propagation of the photon through the silicon into another cell and creation of an electron hole pair. It is also possible that photons which initially do not propagate into the direction of other cells are reflected back into the SiPM either at the silicon substrate or the entrance window and trigger a pixel. A third reason for crosstalk is generation of a charge carrier pair in a low field region by the emitted photons and subsequent drift of a charge carrier into a high field region where it triggers an avalanche. These effects have been thoroughly studied recently in [7] and [17]. An emission spectrum of avalanches in silicon is shown in Fig. 2.12. Compared to the photon detection efficiency spectrum in Fig. 2.8 of an SiPM it can be seen that in the wavelength range of where an SiPM is sensitive to photons the emission of photons has reached a non-negligible level. A rough estimation of the emitted photon number may be obtained by approximating the curve's area from 500 nm to 800 nm with a triangle. With an assumed gain of 10^6 of the SiPM, which is a valid value for a 100 µm pixel pitch SiPM, about 4 to 5 photons are emitted per avalanche.

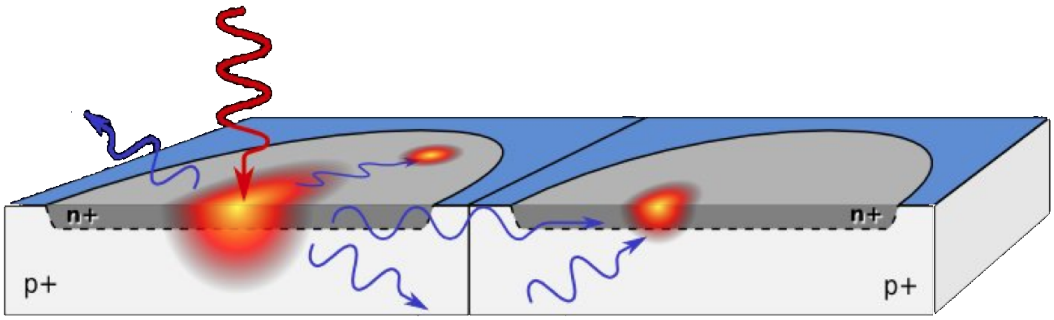

Figure 2.11: Schematic image of optical crosstalk in SiPMs. A photon coming from the initial avalanche enters an adjacent cell and triggers a secondary avalanche. Image adapted from [18].

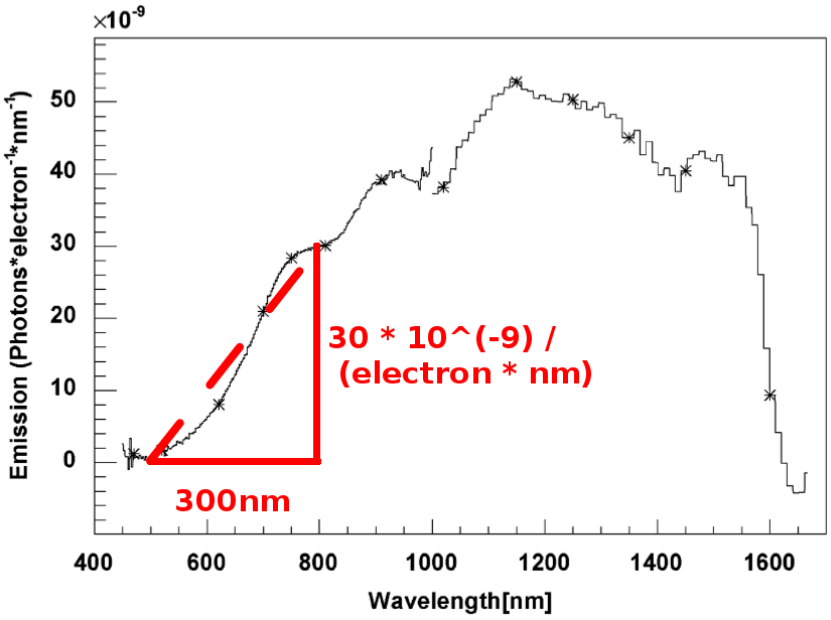

Figure 2.12: Emission spectrum of avalanches in silicon [7]. In the range from 500 nm to 800 nm an SiPM with a gain of 10^6 emits about 4 to 5 photons per avalanche.

3 Simulation Setup

It is very useful to first simulate a practical application of SiPMs inside a detector in order to understand the detector response and to optimize the detector. With knowledge of the properties of the SiPM's operating parameters a precise simulation becomes possible. Thus, an SiPM simulation for the usage in the GEANT4[1] framework was created in [19] and extended in the scope of this thesis.

3.1 GEANT4 Framework

The C++-based and object-oriented simulation framework GEANT4 is capable of simulating particle interactions in matter and is commonly used in high-energy physics as well as in medical physics. It provides a variety of physics modules that may be individually included into simulations. This offers the opportunity to study single contributions of every physical process. However, the user has to provide at least three mandatory C++ classes for GEANT4 to make it work (see [20]). These three classes need to be derived from the following GEANT4 classes, respectively:

- G4VUserPrimaryGeneratorAction
- G4VUserPhysicsList
- G4VUserDetectorConstruction

The G4VUserPrimaryGeneratorAction class holds information about the primary vertex which is the start of the simulation. For this it sends objects of primary particles which contain information about the particle types and their momenta to an event object that is processed by GEANT4. In the G4VUserPhysicsList class the user has to provide the physics processes that are to be simulated in the setup. Here, one may decide whether to simulate all available physical processes or to look at specific contributions of some processes in the simulated setup. The fact that initially no physical process is included into the simulation has the advantage that the simulation time is not unnecessarily increased by physics processes that are not important for the simulation and need not to be simulated. Finally, the G4VUserDetectorConstruction class contains the information about the detector setup that will be simulated. Here, the volumes for the geometry are placed and connected to a material to yield physical behavior of the components. In order to simulate easily an SiPM with its geometry and physical properties in GEANT4 a dedicated SiPM class was designed which will be explained in 3.2.
The workflow of GEANT4 may be described as follows. The simulation starts with

[1] **Ge**ometry **An**d **T**racking

initial particles whose tracks are simulated stepwise and with them possible interactions that may affect the particle's track. The set of interactions which the user wants to simulate have to be defined in the G4VUserPhysicsList class. When, during simulation, a particle hits a sensitive volume, such as later on the SiPM pixel area, a so called hit is created which may contain various information, for example the particle type, momentum or energy of the particle. After completion of the simulation the hits may be digitized by converting the hits into so called digis. The digis are objects that contain in principle the same information as the hits, but the processing of the digis occurs offline, after the simulation. On digitization one may decide whether the hit was valid or not and thus whether the information is to be saved.

3.2 G4SiPM Class

The aim when designing the G4SiPM class was to have a detector simulation of a single SiPM that may be used modularly in any GEANT4 simulation without greater efforts. Hence, with the G4SiPM class it is possible to create an instance of the class and depending on the parameters given to the constructor on invocation the SiPM builds its own geometry according to the required SiPM type. As a part of this thesis the code was extended from merely simulating the SiPM's active area to now including some of the available SiPM housings. For an exemplary image of an SiPM housing in GEANT4 see Fig. 3.1. The green box is what in reality would be the substrate on which the pixels are placed. In the simulation, this is the sensitive detector area which filters the hits with respect to the fill factor. This is done by calculating the nearest pixel center position for each hit and accepting only those events that hit the pixel around an area whose edge length is the pixel pitch times the square root of the fill factor. Hits that fulfilled this requirement are shown in Fig. 3.1 as red dots. Due to the fact, that the pixel position is calculated from the pixel pitch it is possible to simulate virtually any pixel pitch and therefore, the simulation is not limited to the manufactured pixel pitches. Along to the simulation of the SiPM's housing the G4SiPM class also includes noise effects on digitization of the hits.
Yet, the necessary information for this needs to be available for the simulation in an SiPM properties file. The properties file contains the SiPM's breakdown voltage, its thermal noise rate, the afterpulsing probability for the long and the short time constant, the crosstalk probability and the cross talk absorption length, the SiPM's PDE, and the recovery time of the pixels. All parameters may also be given for different operating temperatures. On simulation, a temperature and a bias voltage are assigned to the SiPM and the noise parameters and the PDE are used according to the given operating parameters.
By this it is possible to simulate several SiPMs of various types with different properties for every single SiPM instance. This facilitates the simulation and investigation of varying SiPM behavior similar to differences in real SiPMs of the same type but from a different product line.

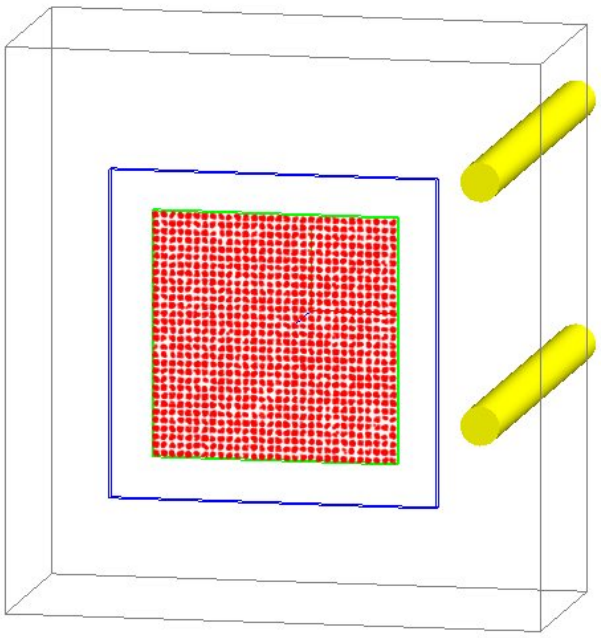

Figure 3.1: Image of a $3{\times}3\,\mathrm{mm}^2$ SiPM from Hamamatsu implemented in the GEANT4 simulation. The area covered with red dots is the active area of the SiPM inside the green box, which represents the sensitive detector. The blue lines mark the entrance window, the black box is the ceramic housing and the electrical connectors are colored in yellow.

3.3 Simulation Program

For verifying the SiPM class a small testing program was written. In this program the particle source is a rectangle that emits photons perpendicular to the SiPM surface in its direction. The starting times of the photons are uniformly distributed as well as the starting positions, which are uniformly distributed over the rectangle's area. When a pixel of the SiPM is hit during the simulation the created hit object contains the information about the time and location of this event.
On digitization, the first action is the digitization of the signal by converting the signal hits to digis. Then thermal noise digis are created that are uniformly distributed over the simulation time interval and the pixels. The noise rate that is used for calculating the appropriate amount of noise events for the simulation time is retrieved from the SiPM's properties file. The digis from both sources are stored in a queue that sorts the digis by their time of occurrence. Afterwards, the program iterates over the queue and filters out all events that happened after a digi event but are still

in the recovery time of the cell. From there on, the afterpulsing and crosstalk events are digitized from the list of already existing digis. The used time constant for the afterpulsing life time is randomized according to the respective probabilities of the short and long fraction and the digi time is randomized according to an exponential decay with the given time constant. The crosstalk digis are created according to the given crosstalk probability in the properties file and the position of a crosstalk digi is randomized with a uniformly distributed ϕ coordinate and an exponentially distributed radius with an absorption length that is also given in the properties file. The resulting queue stores all valid digis that may then be used for further analysis.

4 Measurement Setup

The testing setup may in general be used for various SiPMs. However, in the scope of this thesis three different types of SiPMs were used to demonstrate the feasibility of the procedures. Fig. 4.1 shows two kinds of SiPMs from the manufacturer Hamamatsu where the left SiPM type was mainly used in the scope of this thesis with different pixel sizes. The measurements that were performed with the cooling mount

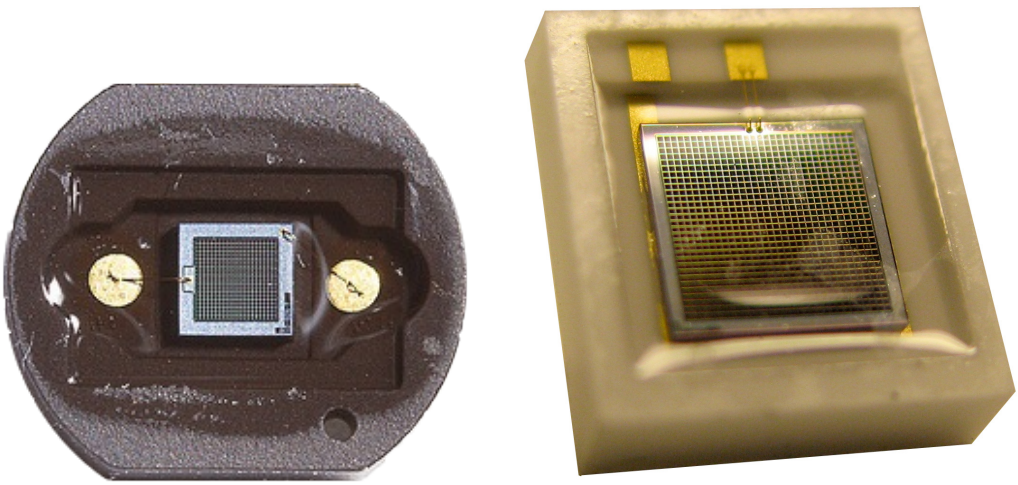

(a) 1×1 mm^2 SiPM with 100 µm pixel pitch. (b) 3×3 mm^2 SiPM with 100 µm pixel pitch.

Figure 4.1: Two SiPM types from Hamamatsu ((a) S10362-11-100C, (b) S10362-33-100C) in ceramic housing with different device sizes. Images from [1] and [21].

had the aim to test its functionality. In future experiments this mount may then be included into the setup of an optical teststand.

4.1 Optical Teststand

The optical teststand was designed in [1] in order to measure several different operating parameters of SIPMs. For this the setup is put under a light-tight box to prevent stray light in general from influencing the measurements. The first thing to measure is an I-V curve of the diode to determine approximately the working point of the SiPM. From there on the dark noise rates for different p.e. thresholds are measured at different voltages and the pulse charge is monitored by the help of a

QDC[1]. From the data taken with the QDC it is possible to determine the per-pixel gain. Having measured this for different overvoltages the gain may finally be used to assess the breakdown voltage by calculating the bias voltage at which the gain reaches theoretically the value 0, i.e. the breakdown of the cell is just about to become possible.
For measuring the relative PDE the teststand uses a white LED. From this the light is guided onto a blazed grating where it is being reflected and diffracted. By the help of a moveable pickup it is possible to select a certain wavelength from the diffracted light with a width of 4 nm. Finally, the light is brought into an integrating sphere to which a calibrated reference light detector (a PIN[2] photodiode) is attached as well as the SiPM that is to be characterized. The integrating sphere is used to diffuse the incoming light and spread it over both detectors isotropically. A major issue in the teststand is the inability to control the temperature of the SiPM. As shown earlier the temperature has a strong influence on the SiPM properties and thus on the results obtained by the teststand. Trying to maintain the room temperature at the same level to reproduce results is an unsatisfactory way. Therefore, a temperature regulation for the SiPM is needed.

4.2 Temperature Regulation and Stabilisation

To stabilize the temperature at the SiPM during the measurements an SiPM mount that fits into the integrating sphere was designed and built in the scope of this thesis. In parallel feasibility studies for the cooling mechanism were performed in [22] and the driver circuit was developed in cooperation.
The general idea of the mount is that a copper plate, inside which is placed the SiPM, is cooled down by using Peltier elements. To vary the cooling power of the Peltier elements, an adjustable constant current source is needed. Furthermore, the temperature needs to be stabilized at a certain setpoint by means of a control algorithm.

4.2.1 SiPM Cooling Mount

The crucial part of the SiPM mount that is responsible for temperature regulation at the SiPM is a copper tube to which is attached a copper plate where the SiPM is embedded. The front plate is shown in Fig. 4.2(c). The inner surface of the copper tube is thermally and electrically insulated by a stable PVC[3] tube. Inside this tube there is the readout electronics for the SiPM on a small amplifier board (see Fig. 4.6) which was designed in the workshop of the III. Physics Institute A. On the outside of the copper tube there is another PVC tube for thermal and electrical insulation. At the end of the copper tube there are copper slabs on either side onto which are mounted Peltier elements with coolers. An aluminum ring around the front part of

[1] Charge (**Q**) to **D**igital **C**onverter
[2] **p**ositive-**i**ntrinsic-**n**egative
[3] **P**oly**v**inyl **c**hloride

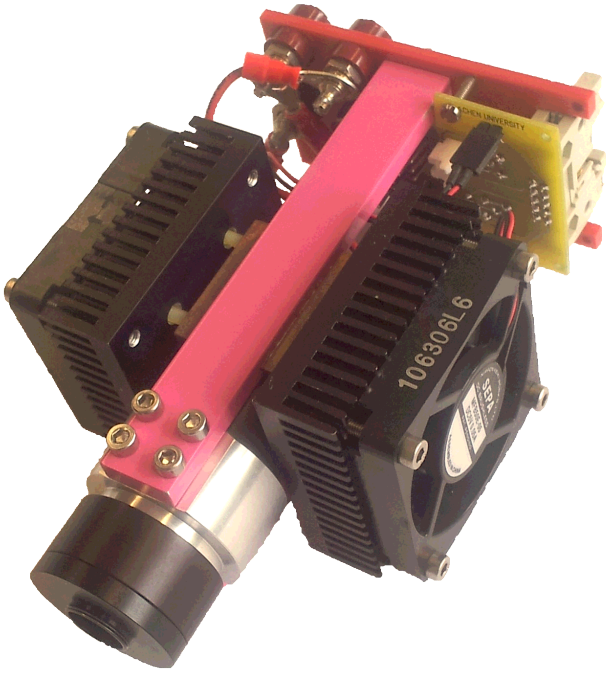

(a) The SiPM mount for temperature stabilization. The front (lower left in the image) is connected to the integrating sphere with the SiPM attached to it. Power supply and signal cables are connected at the rear end. The two fans at the side are cooling the hot sides of the Peltier elements.

(b) Frontplate for the Hamamatsu S10362-11 series.

(c) Frontplate for the Hamamatsu S10362-33 series.

Figure 4.2: (a) Assembled SiPM mount and (b),(c) two front plates for different SiPM types.

the tube provides a threading for an adaptor to couple the device to the integrating sphere. Furthermore, at the sides of the ring two aluminum beams may be attached to carry a backplane which holds connectors for wiring the mount. An exploded drawing of the mount is shown in Fig. C.1 and the assembled SiPM mount is shown in Figures 4.2(a), 4.3 and 4.5. Except for the coolers all parts of the mount were manufactured in the workshop of the III. Physics Institute A.
The SiPM mount is equipped with several DS18B20 [23] temperature sensors that have an absolute accuracy of 0.5 °C and a resolution of 0.07 °C. One of the temperature sensors is placed inside the PVC insulation directly at the front plate to monitor the temperature at the SiPM. The remaining sensors are used to track the temperature at the coolers and the ambient temperature. Another type of sensor that is used in the setup is a DHT22 [24] humidity sensor which is placed at the front of the mount to monitor the relative humidity in the proximity of the SiPM. This is done to prevent the mount from cooling below the dewpoint. Otherwise vaporized water could condensate on the SiPM and influence its performance or possibly destroy it.

The DHT22 has an uncertainty on the measured relative humidity (RH) value of maximum 5 % RH with a resolution of 0.1 % RH, the repeatability of measurements is within 1 % RH.

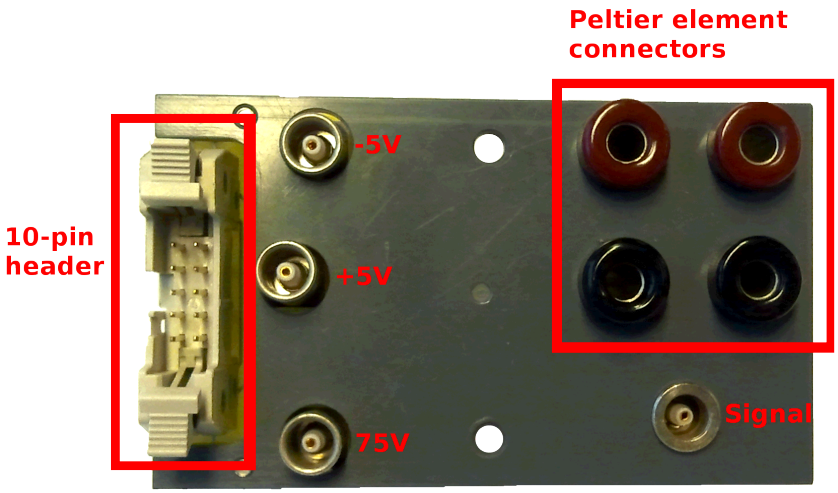

Figure 4.3: Rear view of the SiPM mount. The 10 pin connector on the left is for the power supply of the fans and the readout of the temperature sensors and the humidity sensor. The LEMO connectors labelled 5 V and 75 V are for the amplifier and the SiPM, respectively. The top right connectors are for the power supply of the Peltier elements. The LEMO connector at the bottom right position is for the signal cable. The color differs from Fig. 4.2(a) because the backplane needed to be reproduced.

Peltier Cooling

As described in the setup of the SiPM mount the cooling is established via two Peltier elements. A Peltier element consists of an array of p- and n-doped blocks that are connected via small metal plates. In Fig. 4.4 it can be seen that the transition from n-doped to metal and from metal to p-doped is always on the top side whereas the transitions from p-doped to metal and from metal to n-doped is always on the bottom of the device. When a current flows through the device the electrons coming from the conduction band of the n-doped block are on a higher energy level than the Fermi level in the metal block and the excess energy is converted to heat when dropping from the higher energy level to the lower one. On the other side, when the electrons need to be lifted from the lower Fermi level in metal to the higher n-doped conduction band, thermal energy is used to make the leap between the bands which lowers the temperature at that place. For the p-doped blocks the cold side is at the transition from p-doped to metal and the hot side from metal to p-doped. A more detailed description of the Peltier effect can be found in [22].

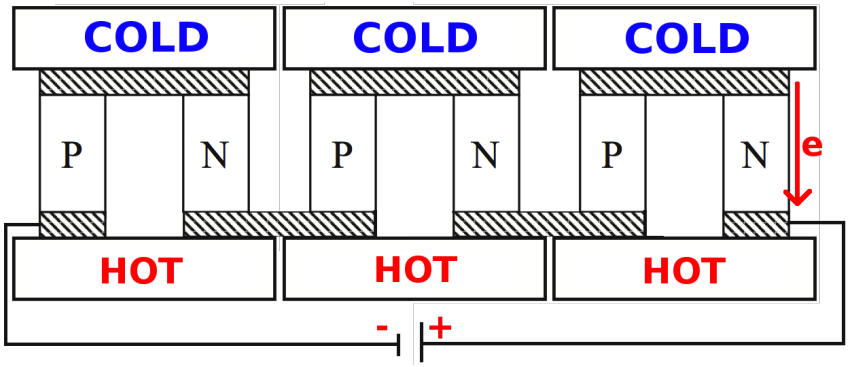

Figure 4.4: Scheme of a Peltier element structure. The cold and hot side may be switched by reverting the current's direction. Image adapted from [25].

As the respective transitions do always happen at the same side of the device a heat transfer through the Peltier element is established. By inversion of the current's direction also the heat flow direction may be inverted. With more current being put through a Peltier element the heat transfer through the device gets larger as well and thus the temperature difference between the two sides of it. From these considerations one can conclude that the minimal absolute temperature that may be achieved with a Peltier element on the cold side is dependent on the ambient temperature.
The two Peltier elements used in the setup may be operated with a maximum current of 8.5 A at a maximum voltage of 3.8 V. The maximum heat per time unit each Peltier element is able to transport is given to be 17.3 W (see [26]). The used Peltier elements were studied in detail in [22].

Backplane

The backplane (Fig. 4.3) of the SiPM mount was designed to connect easily the devices in the mount to the readout and control electronics. For this it has 4 spring connectors for the Peltier elements, two LEMO connectors for the power supply for the amplifier board, one LEMO connector for the bias voltage, one LEMO connector for the SiPM signal, which is spatially separated from the other connectors in order to prevent wrong connections, and a 10-pin header that is used for powering the fans on the coolers and for operating the sensors on the mount.
The temperature sensors communicate via a one-wire bus which means that it is possible to address all sensors via one communication wire since every sensor has its own address. Thus only three paths (GND, +5 V and communication) are used for all sensors. The rear side of the backplane is equipped with a self-designed PCB[4] which is the interface between the connectors on the front and the mount's components, respectively. The PCB offers a three-pin connector for the humidity sensor and eight

[4] **P**rinted **C**ircuit **B**oard

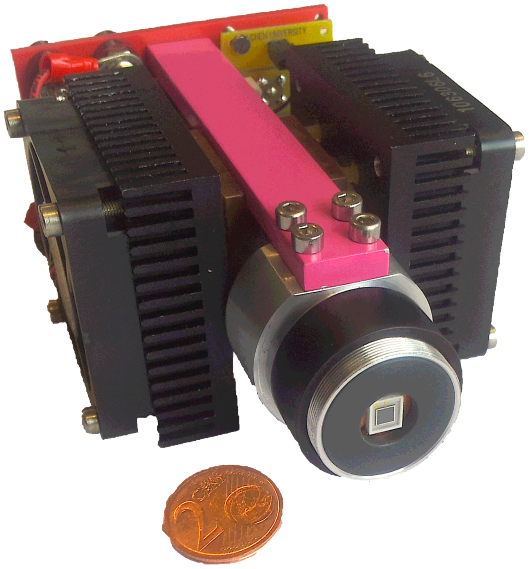

Figure 4.5: The cooling mount with a 3 mm × 3 mm SiPM attached to the front.

three-pin connectors for temperature sensors.

Amplifier

For the application inside the cooling mount, a new amplifier on a small PCB was necessary. This was designed and built by the workshop of the III. Physics Institute

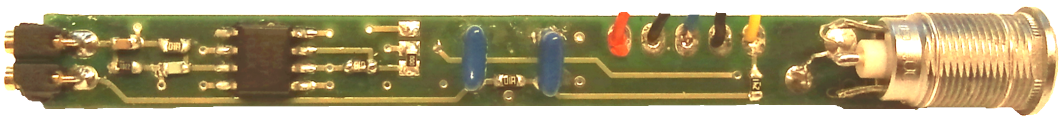

Figure 4.6: The amplifier designed for application in the SiPM cooling mount.

A (see fig. 4.6). It provides the SiPM, which is plugged in at the front, with the operating voltage and features two operating amplifier stages which are non-inverting. A schematic of the amplifier board is shown in D.1. On the back end a LEMO-connector is attached for routing the SiPM signals to the readout electronics, e.g. an oscilloscope. The design gain is at about 100, achieved via an amplification of 10 per stage. However, one has to be careful with the use of this amplifier as it was not fully tested yet and non-inverting amplifiers may tend to oscillate. For the course of the measurements reported in this thesis no oscillations were observed and, thus, the amplifier could be used without any limitations.

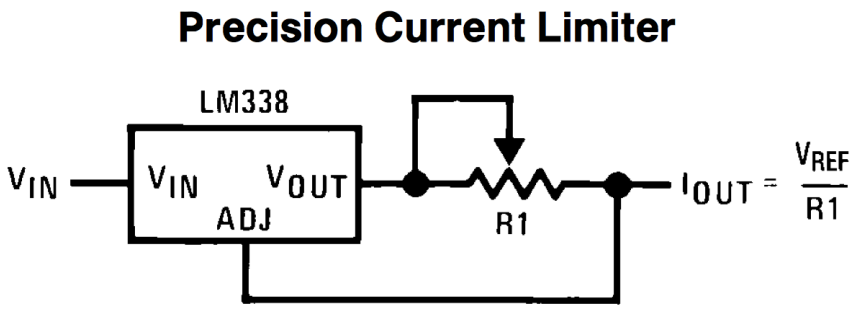

Figure 4.7: Schematic of the constant current operating mode of the LM338T. Schematic taken from [27].

4.2.2 Peltier Controller

For maintaining a certain temperature at the SiPM it is necessary to control the current that flows through the Peltier elements. Thus a PCB was designed with the help of which it is possible to control the current flowing through the Peltier elements from 0 A to 5 A with a resolution of 4 bit. The PCB needs to be connected to a power supply that provides the current and voltage for Peltier element operation and to the Peltier element connectors in Fig. 4.3. A complete schematic of the board is shown in Fig. E.1.
The centerpiece for facilitating the current control is the LM338T chip which is an adjustable voltage supply that is capable of driving up to 5 A. The device maintains a voltage of 1.24 V between its output pin and adjust pin, which may be used to build an adjustable constant current source. A schematic of the necessary circuit to operate the LM338T is given in Fig. 4.7. The adjustable resistor R1 is split into four parallel paths that each contain a resistor and a MOSFET[5] that may be used to close or break the circuit. Fig. 4.8 illustrates this concept. Behind the MOSFETs the four paths are connected to the adjust pin of the LM338T is established. Furthermore the output path is led to the Peltier elements.
With every combination of the activated paths a different output current is needed to reach the 1.24 V adjust voltage and thus the current for the Peltier elements is regulated. The resistors have design values of 0.5 Ω, 1 Ω, 2 Ω and 4 Ω, respectively. This allows for a BCD[6] encoded linear regulation of the current with the possible path combinations. The decision to use MOSFETs instead of usual bipolar transistors was made because of their low maximum internal resistance of only 4 mΩ. By this it is possible to switch the paths electronically without strongly affecting the resulting resistance in the paths. However, bipolar transistors are used to switch the MOSFETs as the control signals arrive on TTL[7] levels, which are 0 V (GND) and +5 V, and the MOSFETs were found to have a sufficiently low internal resistance beginning from

[5] **M**etal-**O**xide **S**emiconductor **F**ield **E**ffect **T**ransistor
[6] **B**inary **C**oded **D**ecimal
[7] **T**ransistor-**T**ransistor-**L**ogic

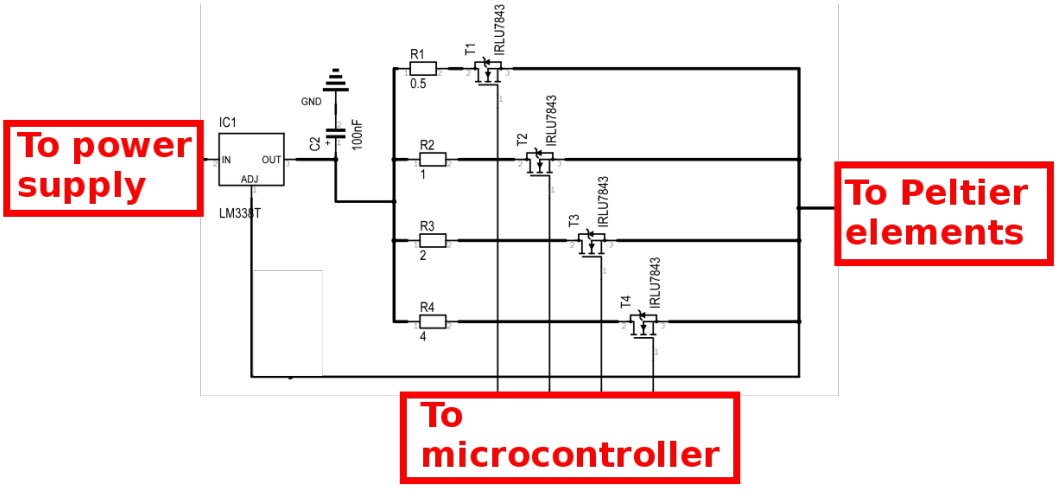

Figure 4.8: Excerpt of the circuit on the Peltier driver PCB. The four resistors and MOSFETs form the adjustable resistor R1 in Fig. 4.7.

+12 V. As the MOSFETs require their operating voltage between gate and source but the gate is at GND potential when the bipolar transistor is active, an inverting Schmitt trigger HEF40106 was included into the circuit to obtain normal behavior again, i.e. a +5 V level on the control wire activates the path of the addressed MOSFET.
As described in 4.2.1, the Peltier elements may be operated with a maximum voltage of 3.8 V. The LM338 requires at least 3 V between its input and output pin to work properly. To fulfill these requirements the board has two spring connectors for the load power source that expect 8 V to 12 V and the connectors for the Peltier elements are put in series in the output path of the LM338. The produced prototype board is shown in Fig. 4.9.

Arduino Mega

On top of the Peltier controller PCB an Arduino Mega board is attached to read out the temperature sensors and to run the necessary control algorithm to stabilize a certain temperature. The board is equipped with an ATMEL ATmega2560 microcontroller. The controller offers 54 digital input/output pins which are not all used, however. The board provides the controller with a clock via a crystal oscillator that has a design frequency of 16 MHz. Furthermore, the board has a USB[8]-to-Serial converter that allows communication between the microcontroller and a connected PC. The used algorithm for the temperature stabilization is a PID[9] control of the current in order to control the temperature at the SiPM. In general a PID controller for temperatures evaluates the offset, also known as error $e(t)$, between the setpoint

[8] **U**niversal **S**erial **B**us
[9] **P**roportional-**I**ntegral-**D**ifferential

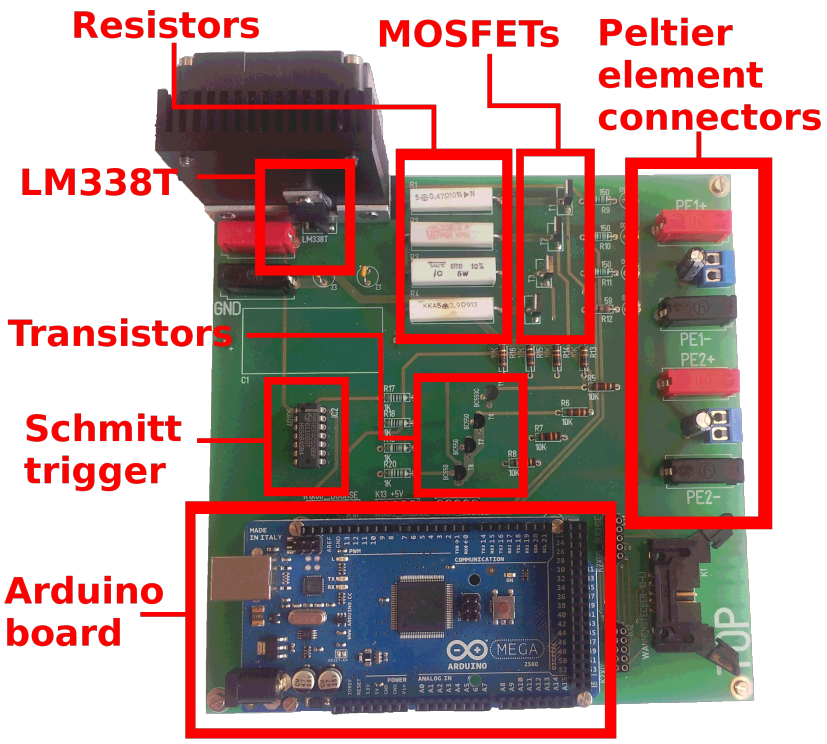

Figure 4.9: Top view of the Controller board for the Peltier elements. On the lower part of the board the Arduino board is attached on top. Note that for the prototype wire connections have to be established from the Arduino to the PCB.

and the actual temperature and calculates an output value $o(t)$ according to the formula:

$$o(t) = k_p \cdot e(t) + k_i \cdot \int_0^t e(t')dt' + k_d \cdot \frac{de(t)}{dt}. \tag{4.1}$$

The factors k_p, k_i and k_d are the gain factors of their respective contributions to the output value where k_p is the gain of the output that is proportional to the error itself, k_i is the gain of the output proportional to the integrated error, and k_d is the gain of the output that is proportional to the change rate of the error, i.e. the derivative. To account for offsets between the reached temperature and the required temperature, which may occur when only the proportional part of the control algorithm is used, the integral part of the control loop is used whereas the derivative is necessary to compensate for disturbances that may rapidly alter the reached temperature.
The PID algorithm on the microcontroller is implemented via a freely available PID library for the Arduino found on [28]. The output value is limited to be from 0 to 15 due to the BCD encoding of the resistor combinations and after calculation of

Setpoint	Uncertainty
20 °C	0.068 °C
15 °C	0.051 °C
10 °C	0.063 °C

Table 4.1: List of the temperature uncertainties for a given temperature setpoint.

the output value the corresponding BCD bit mask is set on four of the Arduino's output pins which form the control lines leading to the Schmitt trigger described earlier. As input for the actual temperature value the board uses the information read from the temperature sensor at the front of the mount. The USB interface of the board is used to manipulate the desired temperature at the SiPM without major efforts as the controller gets the required temperature via USB and does the regulation on its own. Via the USB interface it is also possible to read the actual temperatures from the different sensors and the humidity while measurements at the SiPM are being performed. This is helpful for saving the temperatures and bringing the measurements of the SiPM and the corresponding temperature together later on.

4.3 Temperature Stability

Before the actual measurements on the noise were done, a suitable parameter set for the PID-control needed to be found and the stability of the temperature at the SiPM mount was tested. In [22] a parameter set for a similar model system was proposed and according to this the values 5, 2, and 3 were applied for k_p, k_i and k_d, respectively. While testing different parameter sets it could be seen that for lower temperatures a different set than the one used could yield a slightly more accurate regulation but for simplicity reasons in programming the controller the values were fixed because the difference between the sets is not significant. For the measurements of the temperature stability the mount was set to a certain setpoint temperature and the course of the temperature was monitored over time for 10 minutes. For the lowest temperature of 10 °C for the SiPM studies it was found that the system reached a stable value after ≈ 340 s. The temperature course is plotted in Fig. 4.10 along with the residua. For the setpoints used in the measurements the residual temperatures after 340 s were filled into a histogram to determine the uncertainty of the setpoint temperature (see Fig. 4.11). The uncertainties for each setpoint are listed in Tab. 4.1. The results show that temperature regulation could be achieved to the setpoint with a fluctuation within the resolution of the used temperature sensors.

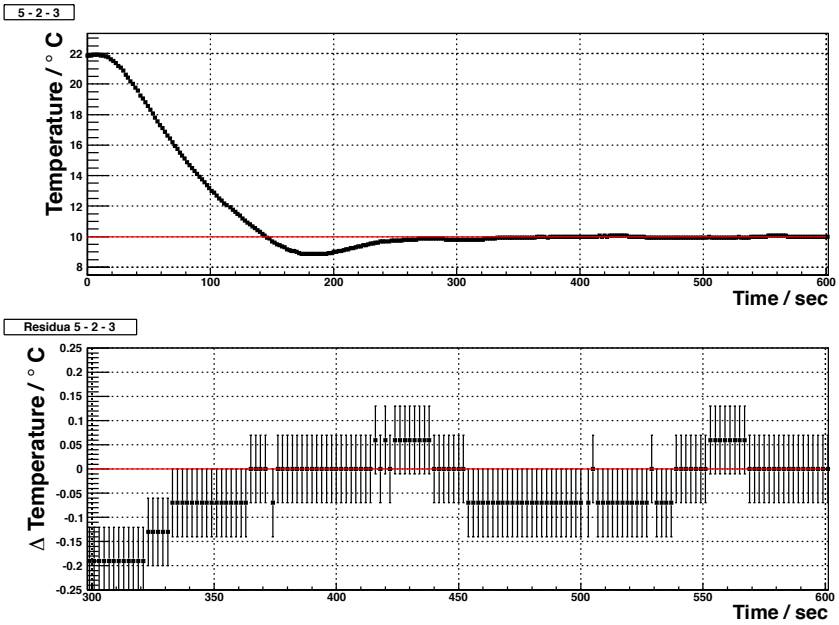

Figure 4.10: Temperature over time for a setpoint temperature of 10 °C. A stable value is reached after about 340 s.

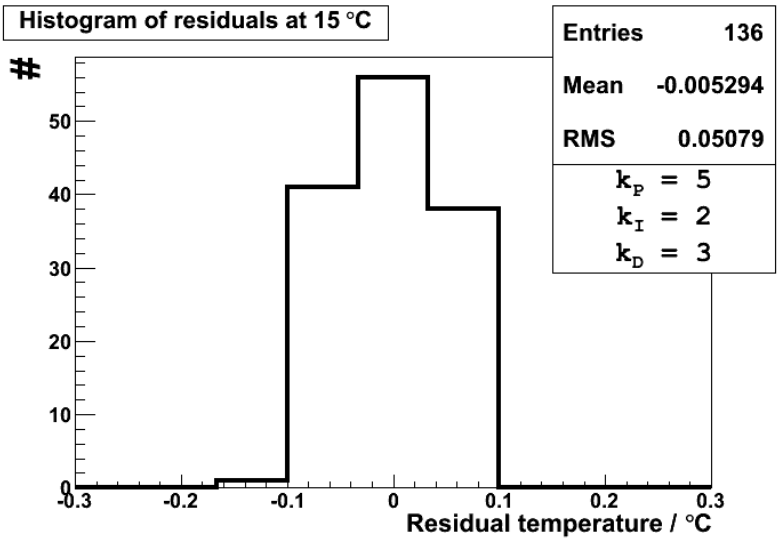

Figure 4.11: Histogram of the residual temperatures for a setpoint temperature of 15 °C after 340 s from start.

5 Measurements at Different Operating Points

For compatibility reasons with the available components of the SiPM cooling mount, the measurements performed in the course of this thesis were done with SiPMs of the Hamamatsu S10362-11 series. Every SiPM is delivered with a recommended operating voltage at a temperature of 25 °C. The manufacturer provides a coefficient that may be used to correct the operating voltage for different temperatures, which is

$$\Delta V = -56 \, \frac{\mathrm{mV}}{\mathrm{K}} \cdot \Delta T. \tag{5.1}$$

Additionally, an approximate value for the breakdown voltage may be calculated by considering that the following holds for the SiPM gain:

$$G \propto \mathrm{V_{OV}} \propto \mathrm{V_{Bias}} - \mathrm{V_{BD}}. \tag{5.2}$$

By setting $\mathrm{V_{Bias}}$ such that the gain is doubled, i.e. the SiPM pulses have twice the original amplitude, one may put the two gains into relation and rearrange the equation as follows

$$\begin{aligned} \tfrac{1}{2} &= \frac{G_1}{G_2} && (5.3)\\ &= \frac{\mathrm{V_{Bias,1}} - \mathrm{V_{BD}}}{\mathrm{V_{Bias,2}} - \mathrm{V_{BD}}} && (5.4)\\ \Leftrightarrow \quad \mathrm{V_{Bias,2}} - \mathrm{V_{BD}} &= 2\mathrm{V_{Bias,1}} - 2\mathrm{V_{BD}} && (5.5)\\ \Leftrightarrow \quad \mathrm{V_{BD}} &= 2\mathrm{V_{Bias,1}} - \mathrm{V_{Bias,2}}. && (5.6) \end{aligned}$$

With this relation it is possible to obtain a rough estimate for $\mathrm{V_{BD}}$ at each temperature for each SiPM used. This was done by using an oscilloscope and setting two bias voltages such that on the second bias voltage the one-p.e. pulse on the oscilloscope is twice as high as on the first bias voltage. The uncertainty for the two voltages is $\sigma_{\mathrm{V_{Bias}}} = 0.1\,\mathrm{V}$ as for a certain voltage the one-p.e. pulses show small fluctuations and the two voltage reference points were chosen by eye on the oscilloscope. The uncertainty on the breakdown voltage was calculated via gaussian error propagation to $\sigma_{\mathrm{V_{BD}}} = 0.22\,\mathrm{V}$. Tab. 5.1 lists all the parameters for the used SiPM types at given temperatures.

5.1 Measurements

5.1.1 I-V Scan

As a first measurement to visualize the temperature dependence of the SiPM's breakdown voltage, an I-V scan was performed for the SiPMs at different temperatures. For this the SiPM is stabilized at a certain temperature and a Keithley

SiPM type	Temperature / °C	$V_{OP}(T)$ / V	$V_{BD}(T)$ / V
Hamamatsu S10632-11-100 $V_{OP,25\,°C}$ = 70.19 V	20	69.91	68.90 ± 0.22
	15	69.63	68.62 ± 0.22
	10	69.35	68.31 ± 0.22
Hamamatsu S10632-11-50 $V_{OP,25\,°C}$ = 70.79 V	20	70.51	69.10 ± 0.22
	15	70.23	68.97 ± 0.22
	10	69.95	68.56 ± 0.22
Hamamatsu S10632-11-25 $V_{OP,25\,°C}$ = 71.74 V	20	71.46	68.90 ± 0.22
	15	71.18	68.96 ± 0.22
	10	70.90	68.44 ± 0.22

Table 5.1: List of SiPM types that were analyzed along with the temperatures during measurements, the recommended operating voltage and the applied voltage corrected for the temperature.

2400 SourceMeter is used to measure the dark current through an SiPM at a specific voltage which is stepwise risen from 67 V to 76 V. The measurement program was developed in the scope of [1]. As one can see in Fig. 5.1(a), a strong rise in the dark current through the SiPM is reached for all temperatures. However, in the case of the 10 °C measurement, this rise occurs between 69 V and 69.25 V whereas for the 20 °C measurement this happens between 69.50 V and 69.75 V. From this one can conclude that the breakdown starts for lower temperatures at lower voltages and, thus, the breakdown voltage decreases with falling temperature. The same tendency may be seen in all of the used SiPM types (see Fig. A.1 and Fig. A.2). This may be explained by the increasing mean free path for an electron in the crystal lattice with falling temperatures as the atom's oscillations become smaller. Hence, it is easier for electrons to gain enough energy to cause charge carrier multiplication before colliding with another atom of the lattice.
Moreover, it may be seen in Fig. 5.1(b) that the operating voltage lies systematically higher for the smaller pixel pitches. Together with Tab. 5.1 it may be found that for smaller pixel pitches the required overvoltage for SiPM operation is larger. The average overvoltage for a 100 µm pixel pitch is at 1.02 ± 0.38 V whereas for a 25 µm pixel pitch the average overvoltage rose to 2.41 ± 0.38 V. This might be explained by the smaller pixel volume which, thus, contains less electrons and the chance that an avalanche is triggered in the device by an electron decreases.

5.1.2 Voltage Trace Analysis

The next step was the analysis of voltage traces that were recorded with a LeCroy WaveJet 354 oscilloscope. The main part of the analysis program for the voltage traces was developed in [29] and was extended in the scope of this thesis to determine the noise rates for different photon equivalents and to acquire sufficiently large statistics. The working principle of the program is as follows. First, a voltage trace

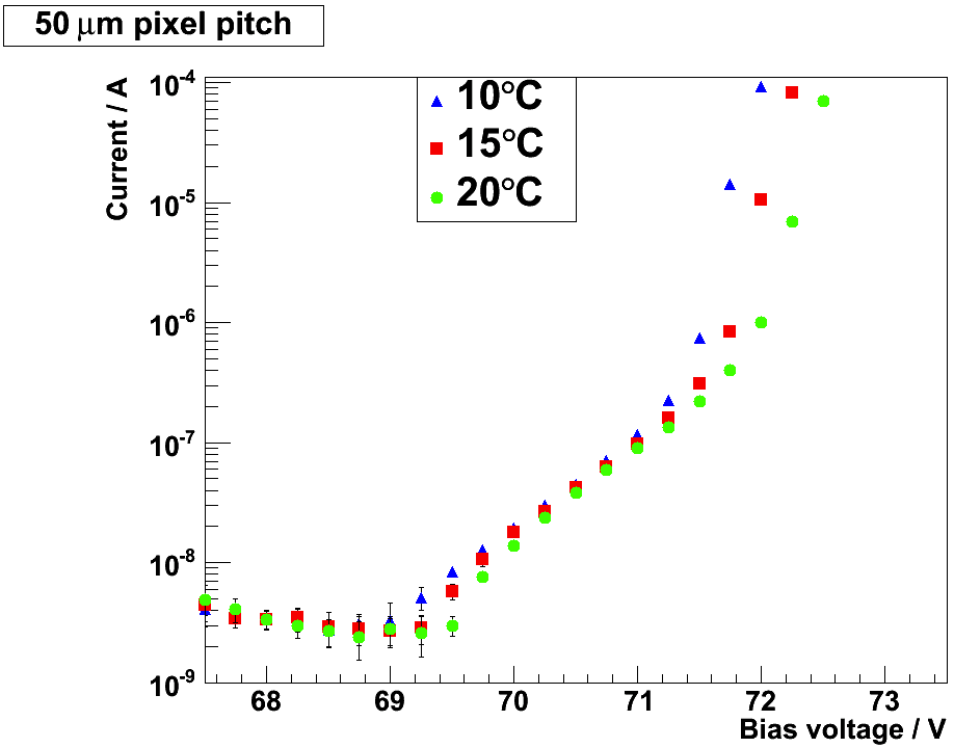

(a) I-V scan for 50 µm pixel pitch at different temperatures.

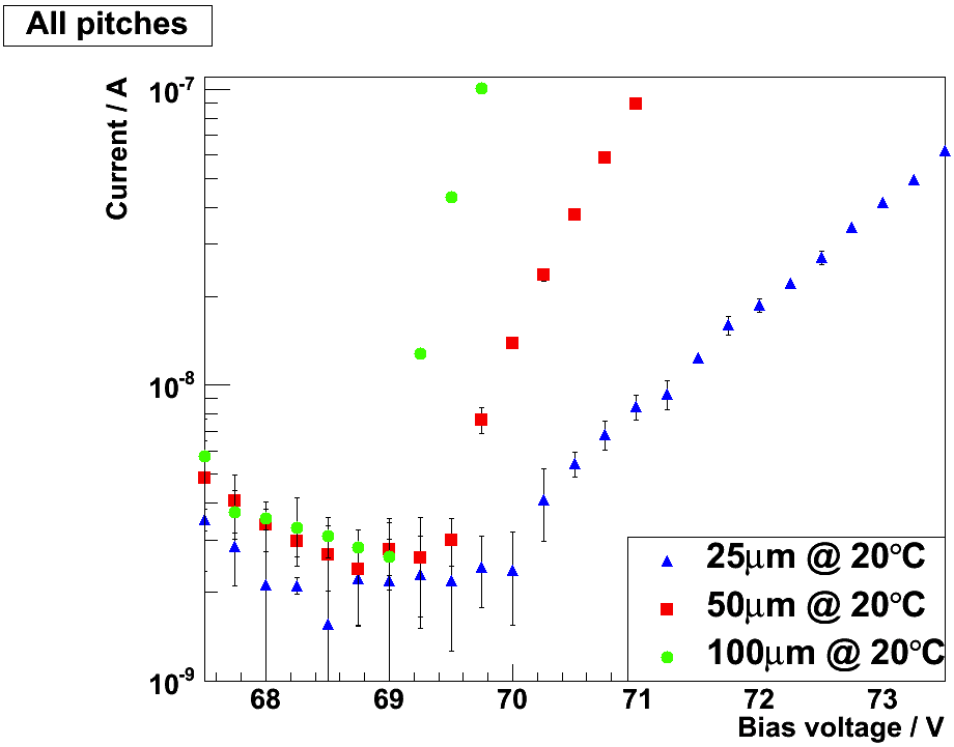

(b) I-V scan for different pixel pitches at 20 °C.

Figure 5.1: I-V scans for (a) 50 µm pixel pitch at different temperatures and (b) different pixel pitches at 20 °C.

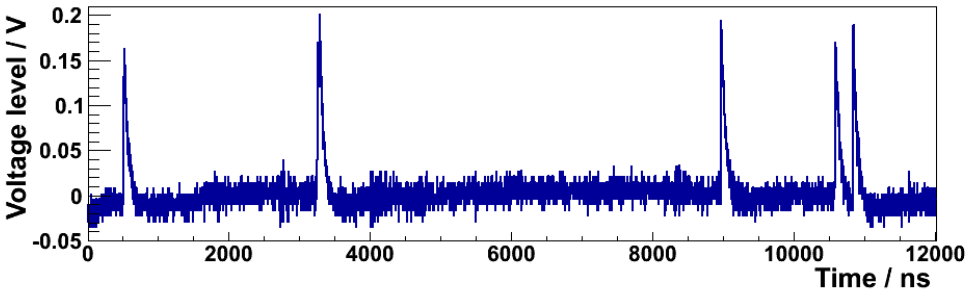

Figure 5.2: Excerpt of a voltage trace recorded with the oscilloscope from a 100 µm pixel pitch SiPM at 20 °C.

with 500000 sample points over 500 µs is recorded with the oscilloscope. Fig. 5.2 shows a recorded sample trace with a total length of 12 µs. Clearly visible are the pulses that stem from single pixel discharges.
After recording the train the program marks positions in the train where the numerical derivative exceeds a certain threshold and is not followed by a larger value within a specific dead time. The threshold value needs to be adjusted for each pixel pitch and may be estimated by dividing the amplitude of a one-p.e. pulse by the rise time of the pulse and using a fraction of the result to be sure to get all peaks. The dead time should be a little larger than the rise time of the pulses but on the same order of magnitude in order to be sure to detect the maximum of a pulse but not to miss subsequent pulses on the tail of the previous one.
With the list of peaks in the derivative of the train the program tests whether in the original train a pulse may be found that is above a trigger threshold and not followed by a larger pulse within the dead time. Here, the threshold needs to be adjusted such that it is far lower than the one-p.e. pulse but not so low that it is triggered by noise. The resulting list of peaks is then filtered for pulses that are not preceded by another pulse for 200 ns. The two lists are then used to plot a histogram of the time difference between two peaks. It is then possible to fit a function to the histogram to determine the afterpulsing time constants and the afterpulsing probability. The fit function is shown in eq. 5.7 and Fig. 5.3 shows a histogram of the peak times with the fitted function.

$$h(t) = a \cdot e^{-\frac{t}{b}} + c \cdot e^{-\frac{t}{f}} + g \cdot e^{-\frac{t}{h}} \tag{5.7}$$

Each fit yields three time constants, b, f and h, of which the largest one is the time constant of the noise in the tail of the plot and the other two are the long and short time constant of the afterpulsing.
In a last analysis step the program performs a threshold scan on the data by counting the pulses above a certain threshold voltage (see Fig. 5.4) and calculates the weighted derivative of the threshold scan by subtracting the trigger rates next to a value and dividing them by their difference in the threshold voltage. The resulting value is

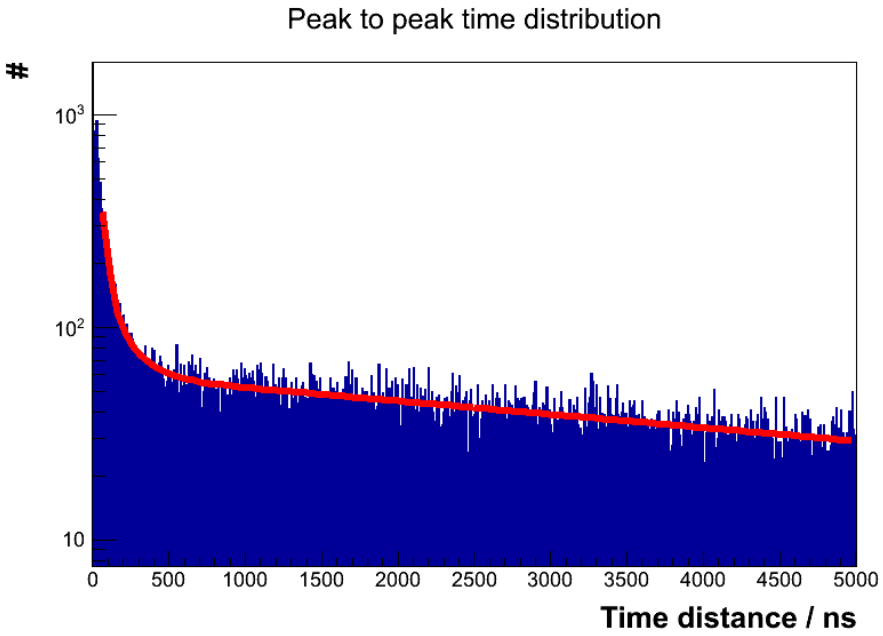

Figure 5.3: Histogram of the time differences between two adjacent peaks. The red line is the fitted function from eq. 5.7.

then weighted with the original triggering frequency (see eq. 5.8).

$$\frac{1}{\text{f(i)}} \cdot \frac{\text{df(i)}}{\text{dU}} = \frac{\text{f(i+1) - f(i-1)}}{\text{U(i+1) - U(i-1)}} \tag{5.8}$$

The reweighting of the derivative is necessary to compensate for the development of the count rate over several orders of magnitude. This helps determining the minima in the differential threshold scan because these are the points where the trigger rate changes most rapidly and their respective threshold voltages correspond to the pulse heights of a specific number of firing pixels. After finding the approximate position of the minima in the differential threshold scan a fit according to

$$g(U) = a \cdot U^2 + b \cdot U + c \tag{5.9}$$

is applied to a narrow region around the minima in the differential threshold scan and the parameters retrieved are used to determine the exact minimum position. To account for any offsets the threshold voltage values of two adjacent minima are subtracted and yield the voltage of a p.e. step. As an upper estimate[1] of the uncertainty of the p.e. step, the distance of the two data points next to the evaluated minimum is taken. Because of the step width for the threshold scan in the software, the uncertainty on a determined p.e. step calculates to about 3 mV^2. Due to the robustness

[1] The fitted parabola serves as an aid to find the minima positions and does not describe the graph's shape. Hence, error propagation on the minima positions leads to too large uncertainties.

[2] Exact value is 2.83 mV

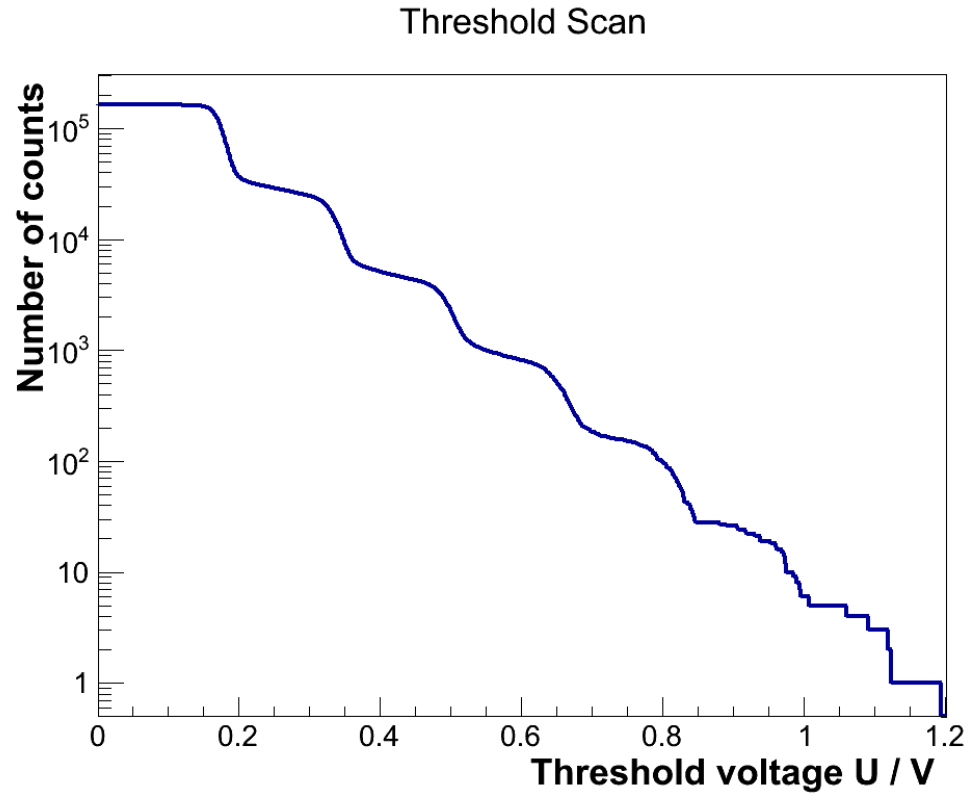

(a) Threshold scan

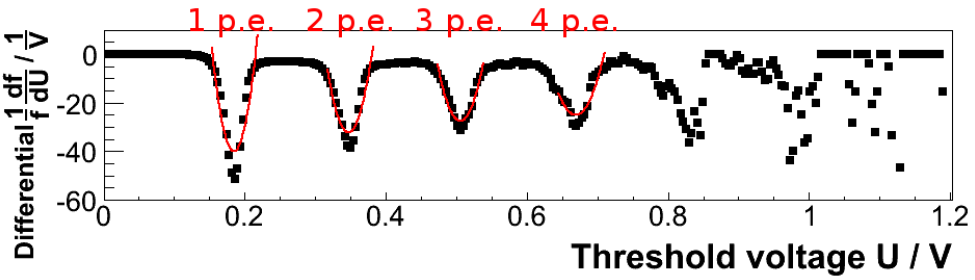

(b) Differential threshold scan

Figure 5.4: Threshold scan and differential threshold scan for a 100 µm pixel pitch SiPM at a temperature of 20 °C with adapted bias voltage. For this setup the minima determination worked most stable.

Pixel pitch / µm	κ
100	1.170
50	1.080
25	1.039

Table 5.2: List of the crosstalk correction factor to account for cells with less neighbors for three pixel pitches.

needed by automatization of the measurement it was only possible to use the first two minima for the p.e. step determination because for higher threshold voltages the algorithm for the minima calculation became unstable due to low statistics for smaller pixel pitches.
From the calculated p.e. step the dark noise rates are calculated by dividing the number of pulses above the 0.5 p.e. threshold voltage by the measurement duration. The crosstalk probability is evaluated by dividing the number of entries above a threshold of 1.5 p.e. by the number of entries above the 0.5 p.e. threshold. This yields the probability that a firing pixel triggers one or more additional pixels. Furthermore, the simulation requires the probability that a fired pixel emits exactly one crosstalk photon. This information is also obtained from the threshold scan in analogy to the overall crosstalk probability. To get the probability one needs to divide the number of pulses with an amplitude of two p.e. by the number of pulses with one or two photon equivalents. The number of pulses with one or two p.e. is calculated by subtracting the entries in the bin of the threshold scan above the 2.5 p.e. threshold from the number of entries that have an amplitude above the 0.5 p.e. threshold. The number of pulses with two p.e. amplitude is calculated by subtracting the number of entries above the 2.5 p.e. threshold from the number of entries above the 1.5 p.e. threshold. For the dark noise rate as well as for the crosstalk probability the uncertainty is propagated from the square root of the number of entries in the respective bins while the uncertainty from the time measurement of the oscilloscope is negligible as it is only 10^{-5} per measured value.
The obtained crosstalk probabilities are averaged crosstalk probabilities over all pixels of the SiPM. Yet it has to be respected that the pixels on the edges and in the corners have less neighbors than the pixels in the middle and, therefore, have a smaller probability to produce crosstalk. To account for this effect, the crosstalk probability needs to be reweighted by a correction factor κ. This is calculated by eq. 5.10.

$$\kappa = \frac{8 \cdot \mathrm{N_{edge}} \cdot \mathrm{N_{edge}}}{4 \cdot 3 + (\mathrm{N_{edge}} - 2) \cdot 4 \cdot 5 + (\mathrm{N_{edge}} - 2) \cdot (\mathrm{N_{edge}} - 2) \cdot 8} \tag{5.10}$$

$\mathrm{N_{edge}}$ is the number of pixels on the edge of the SiPM, which is for quadratic geometries the square root of the pixel number. Including the neighboring pixels at the corner of a pixel, it is possible that a pixel has a maximum of eight neighbors. This applies for all pixels except those on the boundary of the SiPM. The four pixels in the corners have each three neighbors and the pixels on the edge are surrounded

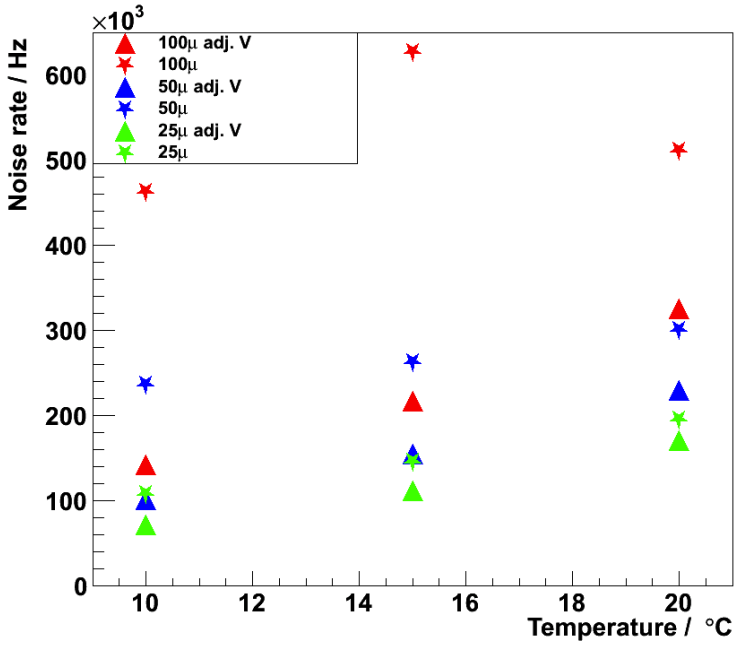

Figure 5.5: Measured dark noise rates over temperature for different pixel pitches once with V_{Bias} adjusted to the temperature (triangles) and once at the recommended operating voltage at 25 °C (stars). For the adjusted voltages the SiPMs are operated at averaged overvoltages of 1.02 V (100 µm), 1.35 V (50 µm), and 2.41 V (25 µm).

by 5 neighbors. κ is listed for each SiPM pixel pitch in Tab. 5.2. The value of the correction factor decreases with increasing pixel number which is expected as the fraction of pixels on the boundary gets smaller as well. However, the equation for κ is a first order approximation under the condition that a crosstalk photon cannot reach further than the direct neighboring pixels which is a reasonable assumption for not too small pixel pitches.
For the dark noise a systematic uncertainty is determined by varying the voltage of a p.e. step by ±0.1 p.e. and calculating the difference in the dark noise rate. The determination of a systematic uncertainty for the crosstalk is done by varying both p.e. step thresholds around ±10 % symmetrically and asymmetrically and taking the largest deviation in each direction as the systematical uncertainty.
Tab. A.1 shows all results obtained from the voltage trace analysis. From the data it can be seen that the dark noise rate at a 0.5 p.e. threshold decreases with temperature for a constant overvoltage as expected. From 20 °C to 10 °C the noise rates have halved for each pixel pitch. In Fig. 5.5 the dark noise rates for the three SiPM types are plotted once with adapted operating voltage and once at the recommended operating voltage at 25 °C. The noise rate for the non-adjusted bias voltage lies systematically higher but shows as well a downwards trend for falling temperatures

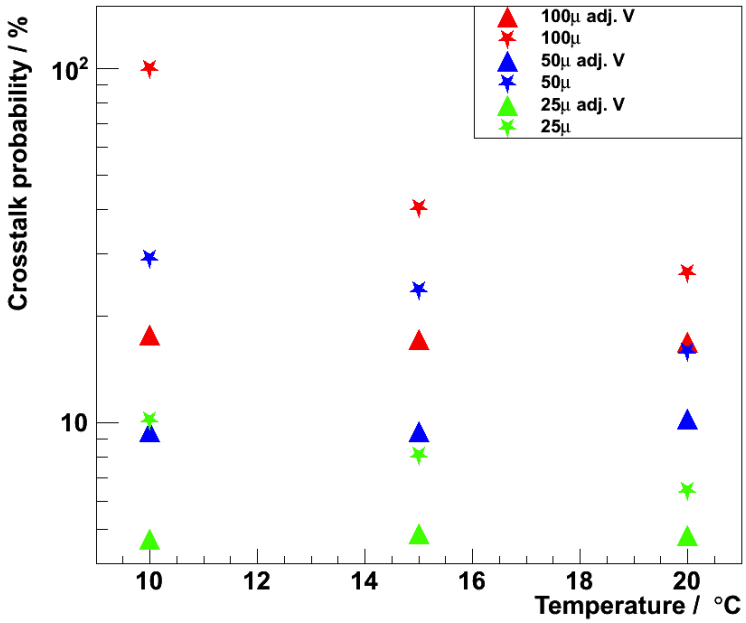

Figure 5.6: Measured crosstalk probability over temperature for different pixel pitches once with V_{Bias} adjusted to the temperature (triangles) and once at the recommended operating voltage at 25 °C (stars). For the adjusted voltages the SiPMs are operated at averaged overvoltages of 1.02 V (100 µm), 1.35 V (50 µm), and 2.41 V (25 µm).

at the 25 µm and 50 µm pixel pitches. The 100 µm pixel pitch shows a different behavior. However, one has to keep in mind that the relative change of the overvoltage with falling temperature is maximal for this SiPM type and at high overvoltages the SiPM is close to a permanent discharge. Therefore, the results should not be considered too reliable for the 100 µm pixel pitch.
Fig. 5.6 shows the results for the crosstalk probability of the measurements. The crosstalk probability remains within its uncertainty constant over temperature at the same overvoltage which resembles results from other measurements. The probability for 100 µm pixels lies at ≈ 17 % down to approximately 4 % for 25 µm pixels. With larger overvoltage also the crosstalk probability rises. The reason for the higher crosstalk probability is the stronger electrical field in the SiPM cells with higher overvoltage and, thus, the higher gain. The larger number of electrons in the avalanche is responsible for a larger number of produced photons.
For the afterpulsing probability a rise with falling temperature at a constant overvoltage may be noticed as well as a rise of the afterpulsing probability without adapting the bias voltage. The latter rise is steeper which is a strong indication that the afterpulsing probability does depend on the temperature as well as on the overvoltage. In [30] and [31] it was observed that the number of unoccupied trap levels in silicon increases with falling temperatures. This may also hint to a similar effect in the rise

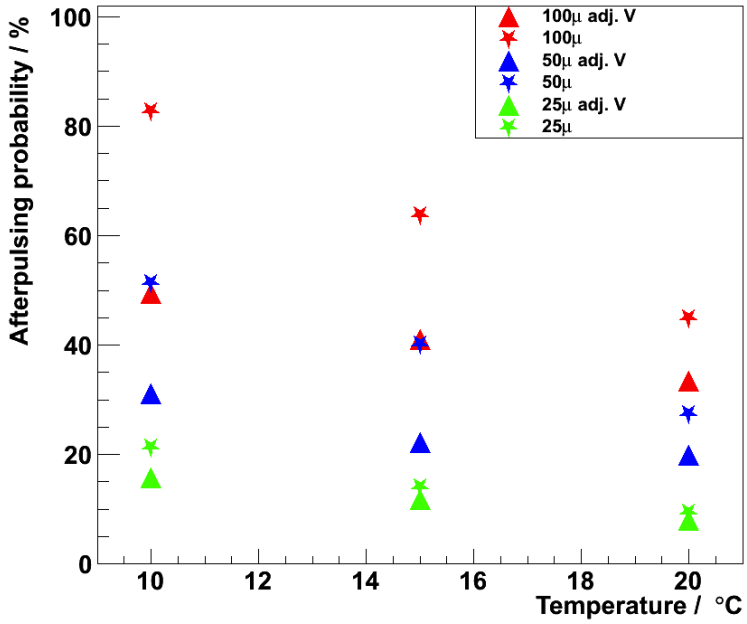

Figure 5.7: Measured afterpulsing probability over temperature for different pixel pitches once with V_{Bias} adjusted to the temperature (triangles) and once at the recommended operating voltage at 25 °C (stars). For the adjusted voltages the SiPMs are operated at averaged overvoltages of 1.02 V (100 µm), 1.35 V (50 µm), and 2.41 V (25 µm).

of the afterpulsing probabilities. The rise of the probability with rising overvoltage could be explained by the greater number of electrons that gain enough energy to occupy the trap levels.
When comparing the results for the afterpulsing probability in [17] to the results obtained in this thesis, it is important to note that the afterpulsing probability in [17] is convoluted with a factor $1 - e^{\frac{t}{\tau_{rec}}}$, where τ_{rec} is the recovery time of the SiPM pixel. This is done to account for diminished pulse heights from retriggered pixels that have not recharged completely, and is necessary in SiPM applications where energy resolution plays a role. In this thesis, the sole probability that on a pixel discharge follows a further pixel discharge of the same pixel due to afterpulsing is calculated. For comparison reasons, in Fig. B.1 the afterpulsing probabilities for a 100 µm pixel pitch SiPM and a 50 µm pixel pitch SiPM from [17] are plotted without convolution.
Tab. 5.3 lists the results from the determination of the p.e. steps. For the cases with adjusted bias voltage the p.e. step for a certain SiPM type stays constant within its uncertainty whereas in the case of a non-adjusted bias voltage the p.e. steps show a tendency towards larger values with falling temperature although the uncertainties would allow for an interpretation as the same value. However, the drift towards larger p.e. steps is expected as the p.e. steps are a measure for the gain of the SiPM

Pixel pitch / µm	**Temperature** / °C	**p.e. step** / mV
adjusted bias voltage		
100	20	162 ± 3
	15	163 ± 3
	10	163 ± 3
50	20	94 ± 3
	15	92 ± 3
	10	92 ± 3
25	20	42 ± 3
	15	42 ± 3
	10	42 ± 3
non-adjusted bias voltage		
100	20	205 ± 3
	15	248 ± 3
	10	fit not possible
50	20	116 ± 3
	15	136 ± 3
	10	152 ± 3
25	20	47 ± 3
	15	52 ± 3
	10	57 ± 3

Table 5.3: Table of the measured p.e. steps for different temperatures with adjusted bias voltage and without adjusted bias voltage.

and as stated earlier the gain is proportional to the overvoltage, which rises with falling temperatures without voltage adjustment. Therefore, the results also show, that for the adjusted bias voltage the SiPM's gain remains constant. In conclusion the performed measurements with the cooling mount delivered reasonable results that are useful for the simulation.

6 Simulation and Comparison

The next step is to set up the SiPM simulation with the previously measured values. Therefore, the simulation was tuned to simulate only noise and no incoming photons. To validate the results coming from the simulation a 50 µm pixel pitch SiPM operated at different operating points was picked and the results of the measurement were implemented into the program.

6.1 Pulse Shape Definition

An easy way to test the simulation performance is to produce simulated traces of the SiPM hits and feed back the generated voltage trace into the analysis framework used in section 5.1. For the pulse shape a template was already included into the simulation program whose parameters needed to be adapted to produce the desired pulse shape. The general formula for the pulse shape over time is

$$f(t) = A \cdot (1 - e^{-\frac{t-t_{start}}{\tau_{rise}}}) \cdot e^{-\frac{t-t_{start}}{\tau_{fall}}}, \tag{6.1}$$

where A is a parameter for the amplitude of the pulse, yet not the amplitude itself, t_{start} is the starting point of the pulse in the time frame of the train, and τ_{rise} and τ_{fall} are the time constants for the rising and the falling edge of the pulse, respectively. The pulse shape is similar to the pulse shape model stated in [32]. However, the pulse shape was adapted as the original shape describes APD pulses but GAPDs produce steeper pulse shapes. In the program the codomain of the pulse is limited to positive values. The values for τ_{rise}, τ_{fall}, and A were determined by searching one-p.e. pulses in the measured trains and fitting the function to them. Tab. 6.1 shows the results of the fits to the pulses of a 50 µm pixel pitch SiPM. The parameters agree within two standard deviations which is expected as the operating voltage for the SiPM was adjusted to the different temperatures and, thus, the overvoltage for the SiPM was held constant. In conclusion it may be seen that the pulse shape does

Temperature in °C	τ_{rise} in ns	τ_{fall} in ns	Amplitude Parameter A in mV
20	3.1 ± 0.3	31.7 ± 2.4	138.7 ± 1.3
15	3.3 ± 0.5	30.0 ± 1.1	145.6 ± 4.4
10	2.8 ± 0.2	29.8 ± 0.6	142.6 ± 4.0

Table 6.1: Parameters for the shape of the one-p.e. pulse of the 50 µm pixel pitch SiPM at different temperatures. The results show good compatibility within their uncertainties.

not show significant changes for different temperatures when the overvoltage is kept constant. A simulated trace is shown in Fig. 6.1(b) next to a trace measured with the oscilloscope. Despite the white noise on the signal in the simulation, which seems

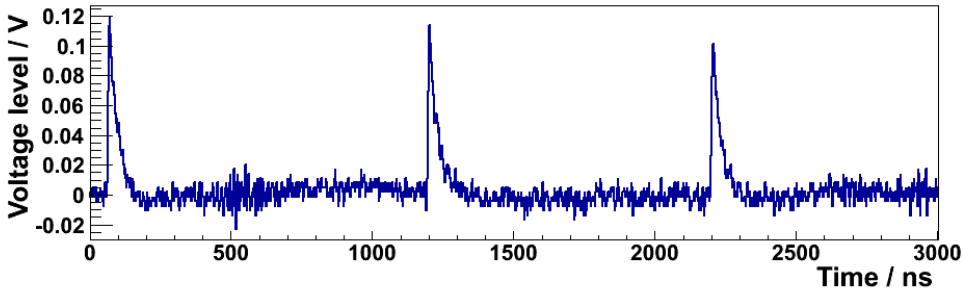

(a) Measured trace

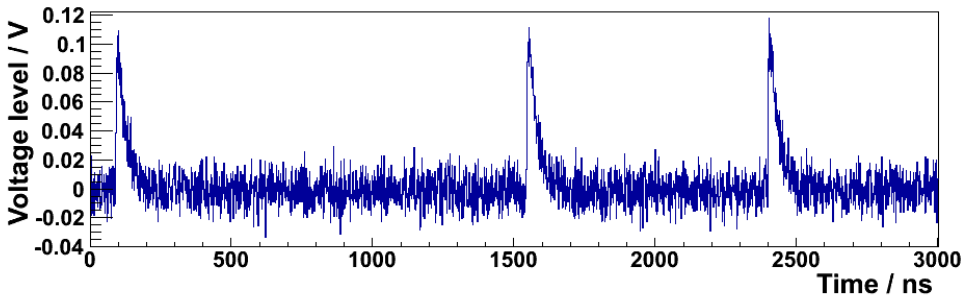

(b) Simulated trace

Figure 6.1: Two voltage traces ($\Delta t \approx 3$ µs), one (a) from measurement with an oscilloscope and one (b) from simulation.

slightly overestimated, the produced signal is consistent with the measured trace. Also one has to keep in mind that the white noise on the signal is an effect of the connected electronics and the simulation would need to be adapted to new electronics to account for the white noise. It has yet to be respected that the simulated trace is the "ideal case" because in contrast to the measured signal the simulated trace shows no digitization effects due to a limited vertical resolution except for the system's numerical accuracy. Furthermore, the simulated traces do not include a possible baseline shift after large pulses. This might become relevant as the SiPM signals are unipolar signals and are likely to draw the amplifier's baseline away from zero if the pulse reaches several p.e. in amplitude.

6.2 Threshold Scan and p.e. Steps

With the ability to generate voltage traces from the simulation the program was run to accumulate an in-simulation time of about 200 ms for 20 °C, 15 °C, and 10 °C. The simulated traces are used to perform a threshold scan and to calculate the weighted differential of the threshold scan as in 5.1.2. The result of the threshold scan for the simulation of the 50 µm pixel pitch SiPM at 20 °C is plotted in Fig. 6.2. The plot in Fig. 6.2(a) show the number of pulses in a time window of 1 ms with event rates normalized to the measurement duration. In the differential threshold scan data (see Fig. 6.2(b)) the p.e. steps are deduced from the distance between the minima. As one may see, the distance between the minima in the simulated data is larger than in the measured data. This leads to a larger p.e. step value in the simulated data.
With the determined p.e. step the dark noise rate of the simulation data is determined in the threshold scan. The lower event number in Fig. 6.2(a) for the simulation data yields a lower dark noise rate in the simulation traces. The results for the p.e. steps and the dark noise determination are listed for all simulated setups in Tab. 6.2. It may be seen that in general the values extracted from the simulation are on

	Measurement		Simulation	
Temp. in °C	Dark noise rate in kHz	p.e. step in mV	Dark noise rate in kHz	p.e. step in mV
20	229.5±0.7	94 ± 3	230.9±0.9	99 ± 3
15	155.2±0.6	92 ± 3	169.3±0.9	97 ± 3
10	101.7±0.5	92 ± 3	123.7±0.8	98 ± 3

Table 6.2: The dark noise rates and the p.e. steps obtained from the measurements and the results of the simulated traces.

the same order of magnitude as the values from measurements. However, the p.e. steps determined in the simulation are systematically higher than the p.e. steps in measurement. An explanation for this might be that, as mentioned earlier, the pulse shape was determined only on a small number of pulses and, thus, the amplitude parameter A may as well be too large. For future simulations it would be useful to be able to extract automatically single p.e. pulses from the train and fit the pulse shape function to these pulses. This could help improving the p.e. step results coming from the simulation.
Regarding the dark noise rate one may see that the dark noise rate can be reproduced for the 20 °C simulation but is about 10 % higher in the case of the 15 °C simulation and about 20 % higher in the 10 °C simulation. A possible explanation of this effect is given in section 6.4.

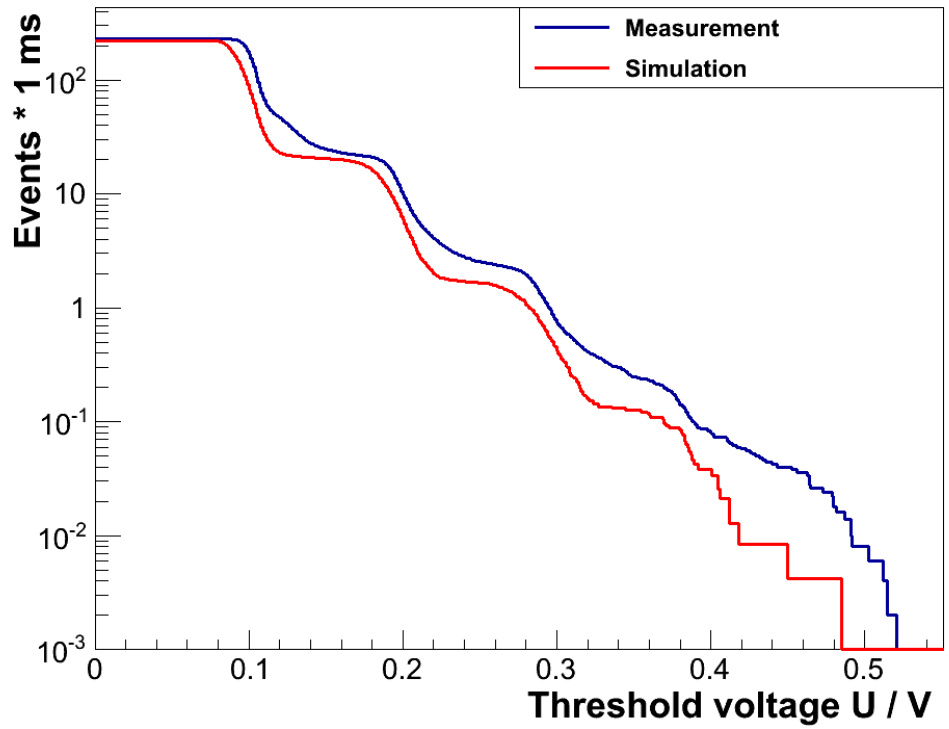

(a) Threshold scan

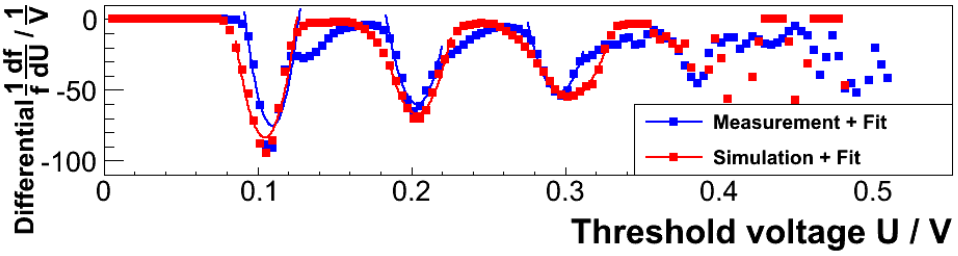

(b) Differential threshold scan

Figure 6.2: (a) Threshold scan and (b) weighted differential threshold scan of the 50 µm pixel pitch SiPM at 20 °C for measurement and simulation. In (b) it is possible to recognize the slightly larger p.e. steps in the simulation from the greater distance between the minima.

6.3 Thermal Noise

After determining the dark noise rate and the p.e. steps the thermal noise rate was determined, which is the rate of avalanches caused by thermal excitation. This quantity is needed to evaluate the number of crosstalk and afterpulsing events as those are generated according to their respective probabilities from thermal noise or physical events. Otherwise the resulting dark noise rate would be too high. The thermal noise rates were obtained from the fit to the peak-to-peak time histogram. There, the inverse of the largest time constant, which comes from the fit at the tail of the histogram, is considered as the thermal noise rate and the two remaining time constants are the time constants of the afterpulsing. Tab. 6.3 lists the noise rates that were determined with the analysis program. The thermal noise rates

	Measurement	Simulation
Temp. in °C	Therm. noise rate in kHz	Therm. noise rate in kHz
20	194.8 ± 7.4	206.0 ± 5.3
15	145.3 ± 7.2	158.0 ± 9.9
10	96.3 ± 8.6	91.8 ± 13.9

Table 6.3: The thermal noise rates from measurement and from simulation.

determined from the simulation agree with the input parameters within about two standard deviations. The relatively large uncertainties on the thermal noise rates for lower temperatures may stem from the fact that the simulated traces contain less pulses due to the lower measured noise rate. Thus, the limited statistics increase the uncertainty on the thermal noise rate, which may be improved by larger in-simulation time. However, the thermal noise rates and the afterpulsing parameters are strongly dependent on each other due to the common fit, and the fact that the thermal noise rate might not be determined correctly, may lead to systematically shifted results in section 6.4.

6.4 Afterpulsing and Crosstalk

After the determination of the p.e. steps and the dark noise rate, the train is analyzed regarding the afterpulsing probability and crosstalk probability. These are determined as described in 5.1.2. The results are listed in Tab. 6.4. As the simulation program requires the single pixel crosstalk probability, both the overall and the single pixel probabilities corrected for the κ factor are listed. It may be seen that the crosstalk probability shows good agreement, except for the results from the 10 °C simulation, where the resulting probabilities are 0.6 percentage points too low for the overall crosstalk probability and 0.4 percentage points too low for the single pixel crosstalk probability. Yet, the results comply within three and two standard deviations, respectively.

Temp. in °C	Overall crosstalk prob. in %	Single pixel crosstalk prob. in %	Afterpulsing prob. in %
measurement			
20	11.3±0.1	10.1±0.1	19.8±0.2
15	10.2±0.1	9.3±0.1	22.2±0.3
10	10.2±0.1	9.3±0.1	31.1±0.5
simulation			
20	10.7±0.1	9.9±0.1	22.2±0.2
15	10.1±0.2	9.4±0.2	31.9±0.3
10	9.6±0.2	8.9±0.2	47.9±0.3

Table 6.4: List of the input parameters for the model and the results of the simulation for the crosstalk probability and the afterpulsing probability. The crosstalk probabilities are corrected for the κ factor.

In contrast to that, the afterpulsing probability constantly lies 2 percentage points to 17 percentage points above the values from measurement. There are two possibilities why this offset may occur. One reason could be that in the fit to the peak-to-peak time histogram the thermal noise component is not exactly determined during the fit. A shift in the time constant of the thermal noise could lead to misidentified fractions of thermal noise and afterpulsing and, thus, systematically affect the afterpulsing probability. The other possible reason could be that the procedure to determine the afterpulsing probability itself is not working properly and produces systematically wrong results. However, this would also mean that the afterpulsing probabilities determined during measurements are as well incorrect. As a crosscheck the simulations were repeated but the effect prevailed. The increased dark noise rate in 6.2 could indeed be explained by an increased afterpulsing probability, which is also supported by the fact that the relative excess in the dark noise rate between simulation and measurement seems to be correlated to the relative excess in the afterpulsing probability. Yet, this would hint to a problem within the simulation.
Concluding, the SiPM model reproduces thermal noise rates, p.e. steps and the crosstalk probability correctly. The dark noise rate and afterpulsing probability show a correct tendency in the results, however, it is still necessary to identify the reasons for the deviations in these quantities. For the crosstalk probability it is important to note that the simulation of crosstalk may only be considered as a first order approximation as the program assumes only one crosstalk photon per crosstalk event which is a reasonable assumption for 50 µm pixel pitch SiPMs. As shown in 2.2.2, an avalanche may produce several photons for a 100 µm pixel pitch SiPM. Studies of the effect on the crosstalk probability in measurement and simulation are still needed.

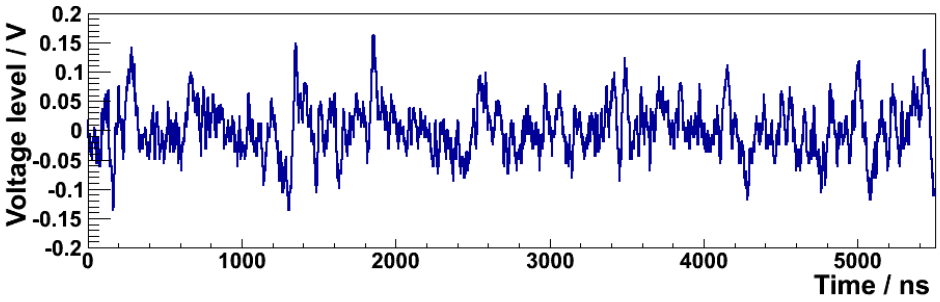

(a) Measured trace

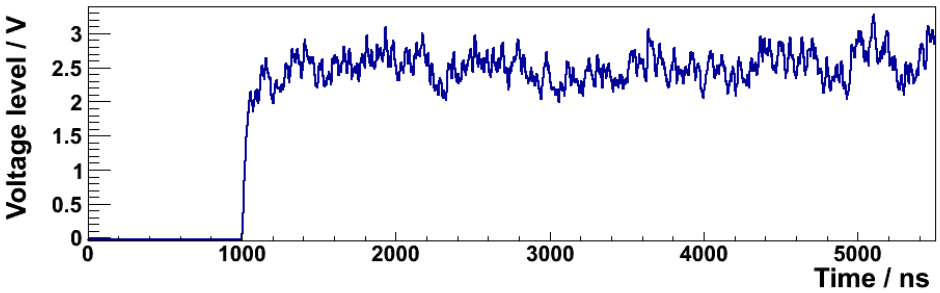

(b) Simulated trace

Figure 6.3: (a) Measured trace of an SiPM exposed to daylight and (b) simulated trace of an SiPM illuminated by 10^5 photons in 1 ns. In both cases it cannot be distinguished between different pulses.

6.5 Saturation Analysis

With the simulation program it was also possible to test the SiPM behavior under illumination. As there were no measurements performed with light sources, this part of the simulation is a qualitative check whether the SiPM shows effects of saturation when the photon flux is large enough. In this part of the simulation a photon source was used. Due to the fact that the simulated SiPM has an active area of 1×1 mm^2 the particle source in the simulation was also set to an area of 1×1 mm^2 to cover the complete area of the SiPM.
Fig. 6.3(b) shows the output trace of a saturated SiPM in comparison to a voltage trace measured with an oscilloscope in Fig. 6.3(a). One sees that it is not possible to distinguish between different pulses. However, the simulated trace shows a voltage level that is on the average different from zero. In reality, the connected readout electronics are not able to sustain the voltage level at the SiPM for long and thus the measured trace oscillates around zero. Fig. 6.4 shows the voltage trace of an SiPM that is illuminated with a pulsed light source for a short time. There, one may see

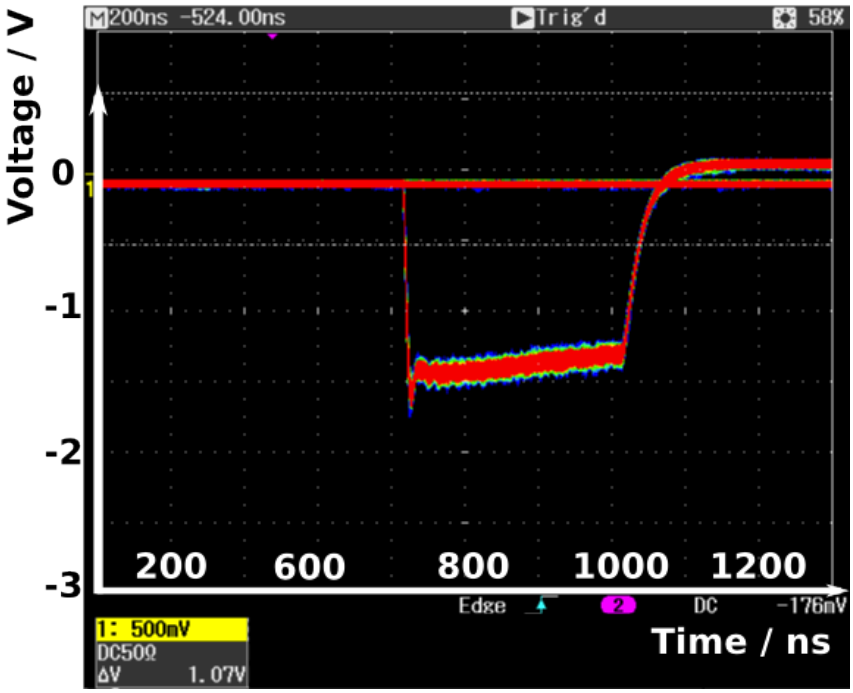

Figure 6.4: Voltage trace of an SiPM blinded with a pulsed light source. A small overshoot is visible at the beginning of the trace. At the end the voltage level drops towards zero. Image from [33].

that at the start of the trace the SiPM shows the same behavior as the simulation. However, it is also visible that the voltage level starts decreasing over time and will eventually reach the 0 V level as in Fig. 6.3(a). In conclusion the plots of the voltage traces show that the SiPM simulation model is capable of simulating the behavior under strong light flux in a short exposure time, yet it has to be studied whether the simulation needs to be adjusted such that the trace voltage level drops to zero or if it is possible to design a supply for the SiPM that may sustain a trace voltage level different from zero. For the latter one has to keep in mind that a too large power consumption might destroy the SiPM. In any case the SiPM is not designed for operation under permanent strong illumination.
For studying the SiPM behavior regarding its linear response to short light pulses, Fig. 6.5 shows a dynamic range scan for a 50 µm pixel pitch SiPM at 15 °C. The simulation was set to emit varying numbers of photons towards the SiPM in time windows of 1 ns and 100 ns. The number of triggered SiPM pixels is plotted against the number of emitted photons in the SiPM's direction along with the fraction of the pixel trigger origin. One may see that first the SiPM's response is linear in Fig. 6.5(a) and Fig. 6.5(b) but the total number of photons when the SiPM starts saturating depends on the time window in which the photons arrive at the SiPM. Furthermore, in Fig. 6.5(c) and Fig. 6.5(d) is visible that for a short illumination

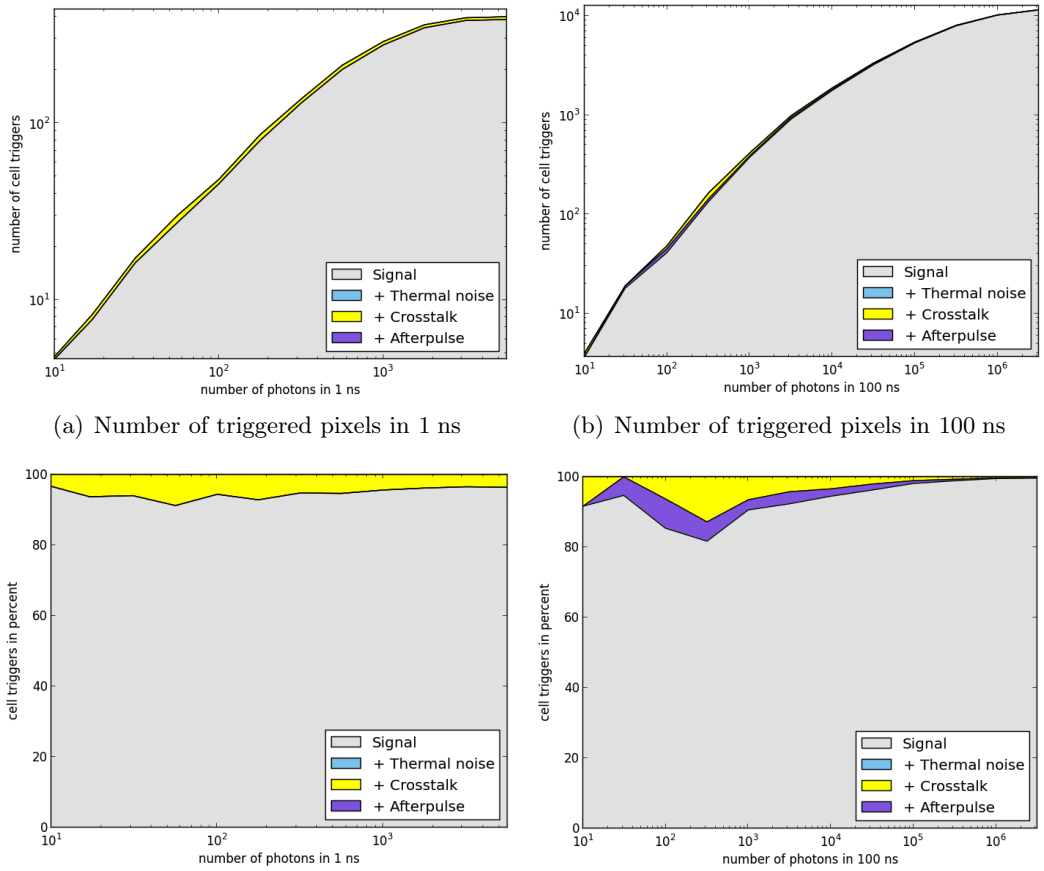

(a) Number of triggered pixels in 1 ns

(b) Number of triggered pixels in 100 ns

(c) Fraction of pixel trigger origins in 1 ns

(d) Fraction of pixel trigger origins in 100 ns

Figure 6.5: Simulated dynamic range of a 50 µm SiPM at 15 °C for an illumination time of 1 ns ((a) and (c)) and 100 ns ((b) and (c)). The number of triggered pixels saturates for too large photon numbers. The cell triggers in percent in (c) and (d) are the fractions of all fired pixels regarding their origins. Images from [33].

time the SiPM shows no contribution from afterpulsing or thermal noise to to the number of pixel triggers. For the long illumination time the afterpulsing fraction gets noticeable. The fact that there are still no contributions from afterpulsing to the pixel triggers in the 100 ns sample is due to the probability of about 1.5 % for a thermal noise event in this time window for a noise rate of 145 kHz. With increasing noise rates also thermal noise events will be noticed. This behavior is similar to the effect shown in 2.9. This shows that the SiPM simulation model resembles the theoretically expected behavior of real SiPMs.

7 Conclusion and Outlook

In the scope of this thesis an SiPM mount for temperature regulation and stabilization was designed and built. Experimental studies of the setup showed that it may be used to cool down SiPMs to temperatures of 10 °C. The required temperature is reached in 5 to 6 minutes and a regulation with a precision better than 0.1 °C is possible over several hours. Theoretically, lower temperatures would be possible, yet the relative humidity of the surrounding air needs to be decreased in order to lower the dew point. Otherwise humidity would condensate on the SiPM and might destroy the device.
Future developments of the SiPM mount should extend the temperature regulation towards active heating via inverting the current through the Peltier element. This would facilitate a faster stabilization of the temperature and might also lead to a more precise regulation.

By now, it is only possible to automatize measurements by sending the microcontroller on the Arduino board the required temperature and pausing the readout for a programmed time that needs to be long enough to allow the system to stabilize. It would be convenient to have an interface between the microcontroller and the connected computer that controls the measurements such that it is possible to set a desired temperature and the microcontroller sends a response when having reached a stable state. For this an upgrade of the firmware on the microcontroller is necessary. Furthermore, a metal box around the setup would shield the SiPM from electromagnetic noise. By grounding the copper tube and the cooling elements the signal to noise ratio was improved but there still remains some noise in the signals that could be eliminated. However, a way to conduct the heat from the warm side of the Peltier elements to the outside of the box needs to be found to avoid overheating of the system.

The analysis of the traces that were recorded with the oscilloscope showed results that are consistent with theory and proved themselves to be useful parameters for the simulation. A parameter set for Hamamatsu SiPMs with pixel pitches of 100 µm, 50 µm, and 25 µm was acquired and is available for future simulations. The simulation itself demonstrates a good performance in simulating the basic features of an SiPM, thermal noise rate and voltage trains, yet it is necessary to study the deviation of the crosstalk probability and the afterpulsing probability and whether this may explain the too large dark noise rate in the simulated traces. Once these problems are solved, the afterpulsing probability could be studied more systematically by analyzing not only peak-to-peak time differences with a one-p.e. initial pulse but also for pulses that are above the 1.5 p.e. threshold in amplitude and for all pulses allowed

as initial pulse. The corresponding afterpulsing probability should be correlated to the type of initial pulse.
Additionally, the SiPM model needs to be extended such that it is possible to give properties files to the simulation and the simulation interpolates between the parameters if the required operating point is not exactly stated in the file. In this context also better interpolation algorithms have to be found and the overvoltage dependency of the SiPM's operating parameters needs to be studied systematically. First analyses regarding this topic are already being performed.

A Additional Tables and Plots

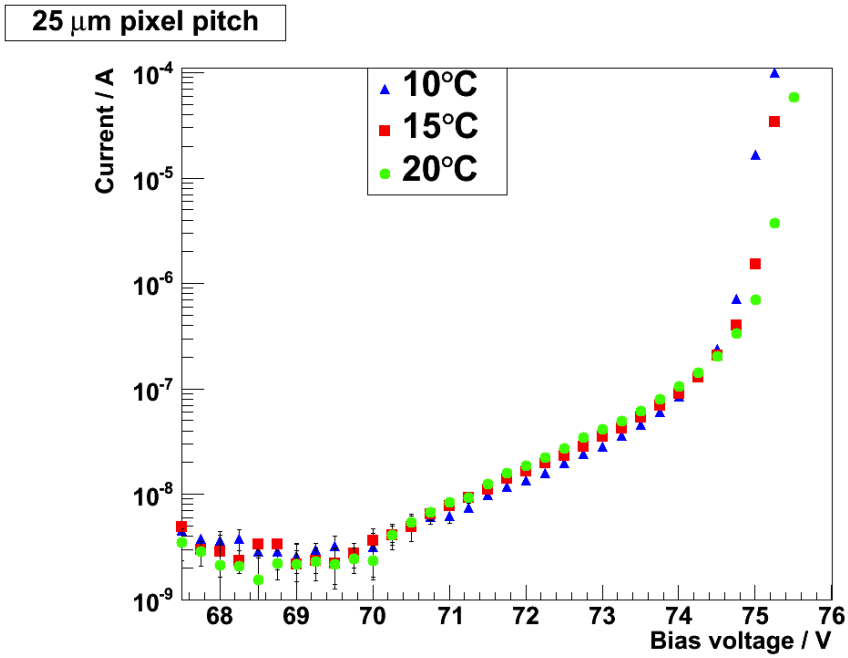

Figure A.1: I-V scan of the 25 µm pixel pitch at different temperatures.

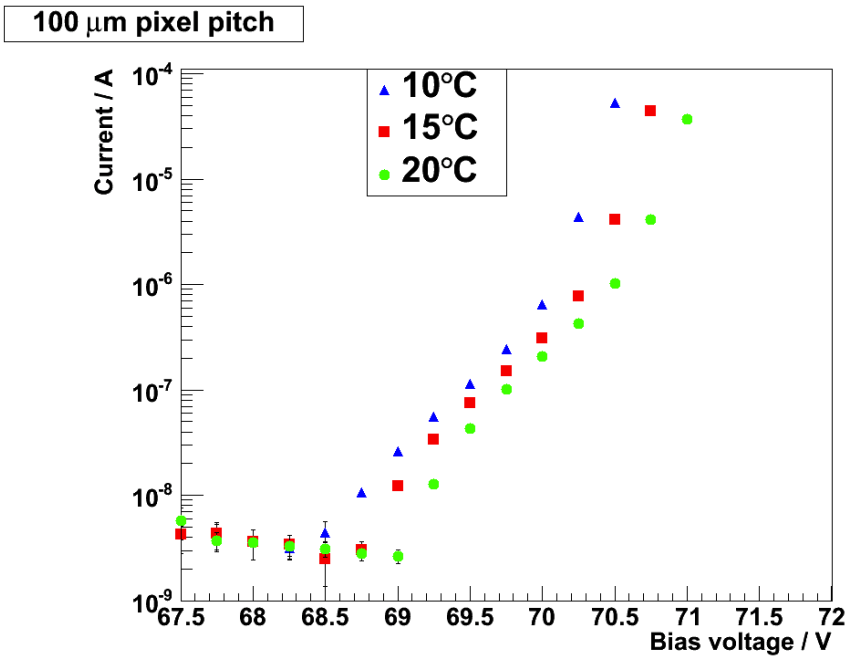

Figure A.2: I-V scan of the 100 µm pixel pitch at different temperatures.

Hamamatsu S10362-11-100 Serial No.: 2588						
T / °C	U / V	0.5 p.e. noise / kHz	CT prob. / %	$\tau_{AP,s}$ / ns	$\tau_{AP,l}$ / ns	AP prob. / %
20	69.91	325.7 ± 0.8 (stat) $^{+0.8}_{-0.6}$(sys)	16.8 ± 0.1 (stat)	46.7 ± 6.2 (stat)	140.1 ± 14.7 (stat)	33.5 ± 0.1(stat)
15	69.63	217.5 ± 0.7 (stat) $^{+0.5}_{-0.4}$(sys)	17.2 ± 0.1 (stat)	54.4 ± 4.5 (stat)	181.3 ± 20.0 (stat)	41.0 ± 0.2(stat)
10	69.35	142.6 ± 0.5 (stat) $^{+0.4}_{-0.3}$(sys)	17.7 ± 0.2 (stat)	57.3 ± 6.4 (stat)	157.8 ± 22.6 (stat)	49.5 ± 0.2(stat)
20	70.19	511.3 ± 1.0 (stat) $^{+3.1}_{-1.6}$(sys)	26.5 ± 0.1 (stat)	54.9 ± 2.5 (stat)	167.6 ± 12.9 (stat)	44.9 ± 0.1(stat)
15	70.19	627.6 ± 1.1 (stat) $^{+12.1}_{-8.9}$(sys)	40.5 ± 0.1 (stat)	45.8 ± 2.3 (stat)	148.9 ± 7.9 (stat)	63.9 ± 0.1(stat)
10	70.19	463.2 ± 1.0 (stat) ± 0 (sys)	100 ± 0.2 (stat)	38.2 ± 1.2 (stat)	153.3 ± 4.5 (stat)	82.8 ± 0.1(stat)
Hamamatsu S10362-11-50 Serial No.: 2102						
T / °C	U / V	0.5 p.e. noise / kHz	CT prob. / %	$\tau_{AP,s}$ / ns	$\tau_{AP,l}$ / ns	AP prob. / %
20	10.51	229.5 ± 0.7 (stat) $^{+0}_{-0}$(sys)	10.3 ± 0.1 (stat)	31.6 ± 4.9 (stat)	127.8 ± 19.2 (stat)	19.8±0.2(stat)
15	70.23	155.2 ± 0.6 (stat) $^{+0}_{-0}$(sys)	9.5 ± 0.1 (stat)	39.5 ± 4.9 (stat)	153.3 ± 31.2 (stat)	22.2±0.3(stat)
10	69.95	101.7 ± 0.5 (stat) $^{+0}_{-0}$(sys)	9.5 ± 0.1 (stat)	29.3 ± 4.9 (stat)	129.5 ± 16.5 (stat)	31.1±0.5(stat)
20	70.79	301.7 ± 0.8 (stat) $^{+0.2}_{-0}$(sys)	16.0 ± 0.1 (stat)	26.7 ± 3.4 (stat)	110.3 ± 9.0 (stat)	27.5±0.2(stat)
15	70.79	263.7 ± 0.7 (stat) $^{+0.4}_{-0.2}$(sys)	23.7 ± 0.1 (stat)	27.6 ± 2.9 (stat)	109.8 ± 7.7 (stat)	40.1±0.3(stat)
10	70.79	237.6 ± 0.7 (stat) $^{+0.6}_{-0.4}$(sys)	29.1 ± 0.2 (stat)	31.3 ± 2.3 (stat)	132.8 ± 9.4 (stat)	51.5±0.3(stat)
Hamamatsu S10362-11-25 Serial No.: 1068						
T / °C	U / V	0.5 p.e. noise / kHz	CT prob. / %	$\tau_{AP,s}$ / ns	$\tau_{AP,l}$ / ns	AP prob. / %
20	71.46	170.7±0.6 (stat) $^{+1.8}_{-0.4}$(sys)	4.8±0.1(stat)	28.8±7.1(stat)	152.6±33.5	8.0±0.2(stat)
15	71.18	111.6±0.5 (stat) $^{+1.2}_{-0.5}$(sys)	4.9±0.1(stat)	28.9±7.5(stat)	148.8±42.5	11.8±0.3(stat)
10	70.90	72.4±0.4 (stat) $^{+0.9}_{-0.2}$(sys)	4.7±0.1(stat)	30.7±10.1(stat)	169.1±48.7	15.7±0.5(stat)
20	71.74	196.6±0.6 (stat) $^{+2.0}_{-0.4}$(sys)	6.5±0.1(stat)	42.7±6.5(stat)	315.3±190.0	9.5±0.2(stat)
15	71.74	146.8±0.5 (stat) $^{+1.3}_{-1.3}$(sys)	8.1±0.1(stat)	32.8±8.0(stat)	160.3±42.8	14.1±0.3(stat)
10	71.74	108.7±0.5 (stat) $^{+0.9}_{-0.8}$(sys)	10.2±0.1(stat)	28.2±7.7(stat)	130.5±27.1	21.3±0.3(stat)

Table A.1: Detailed list of the results obtained from the voltage trace analysis. 0.5 p.e. noise is the dark noise rate of the SiPM, CT prob. is the overall crosstalk probability, $\tau_{AP,s}$ is the short time constant of the afterpulsing, $\tau_{AP,l}$ is the long time constant of the afterpulsing, AP prob. is the afterpulsing probability. The results for the crosstalk probability are not corrected for the κ factor.

B Afterpulsing probabilities

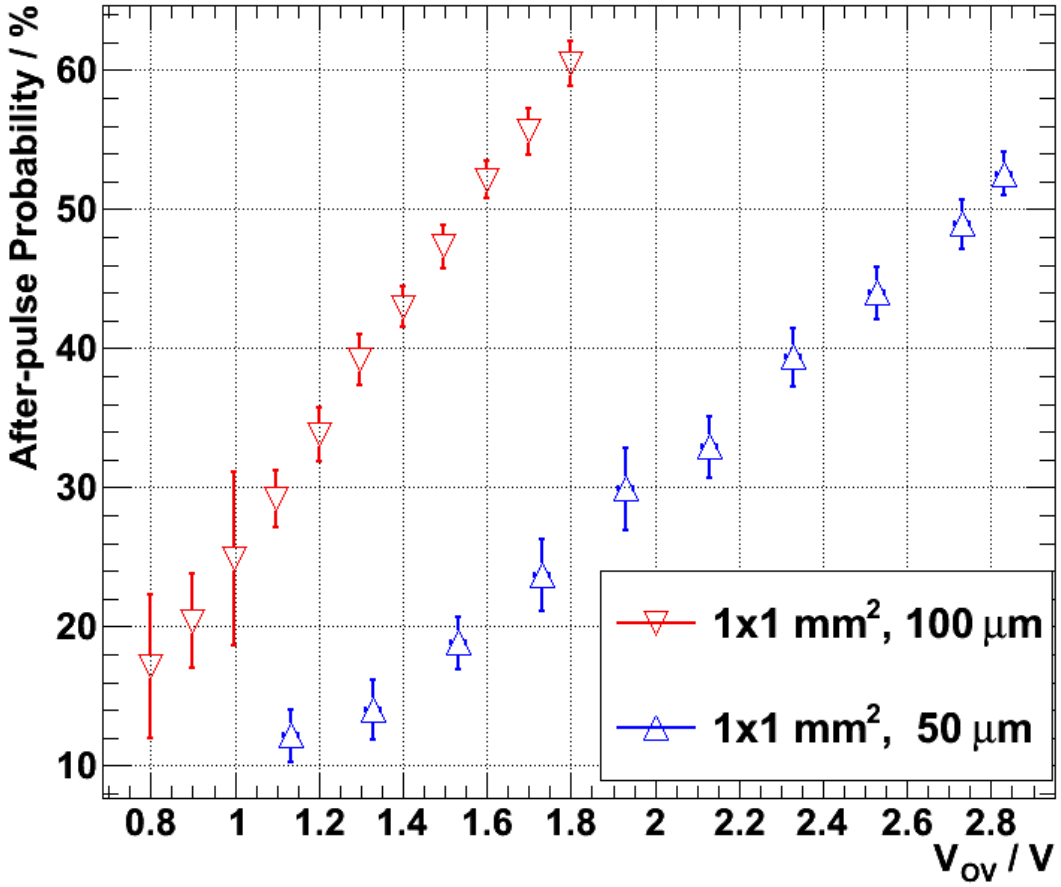

Figure B.1: Afterpulsing probabilities from [17] without convolution. Image from [34].

C Exploded Drawing of the Cooling Mount

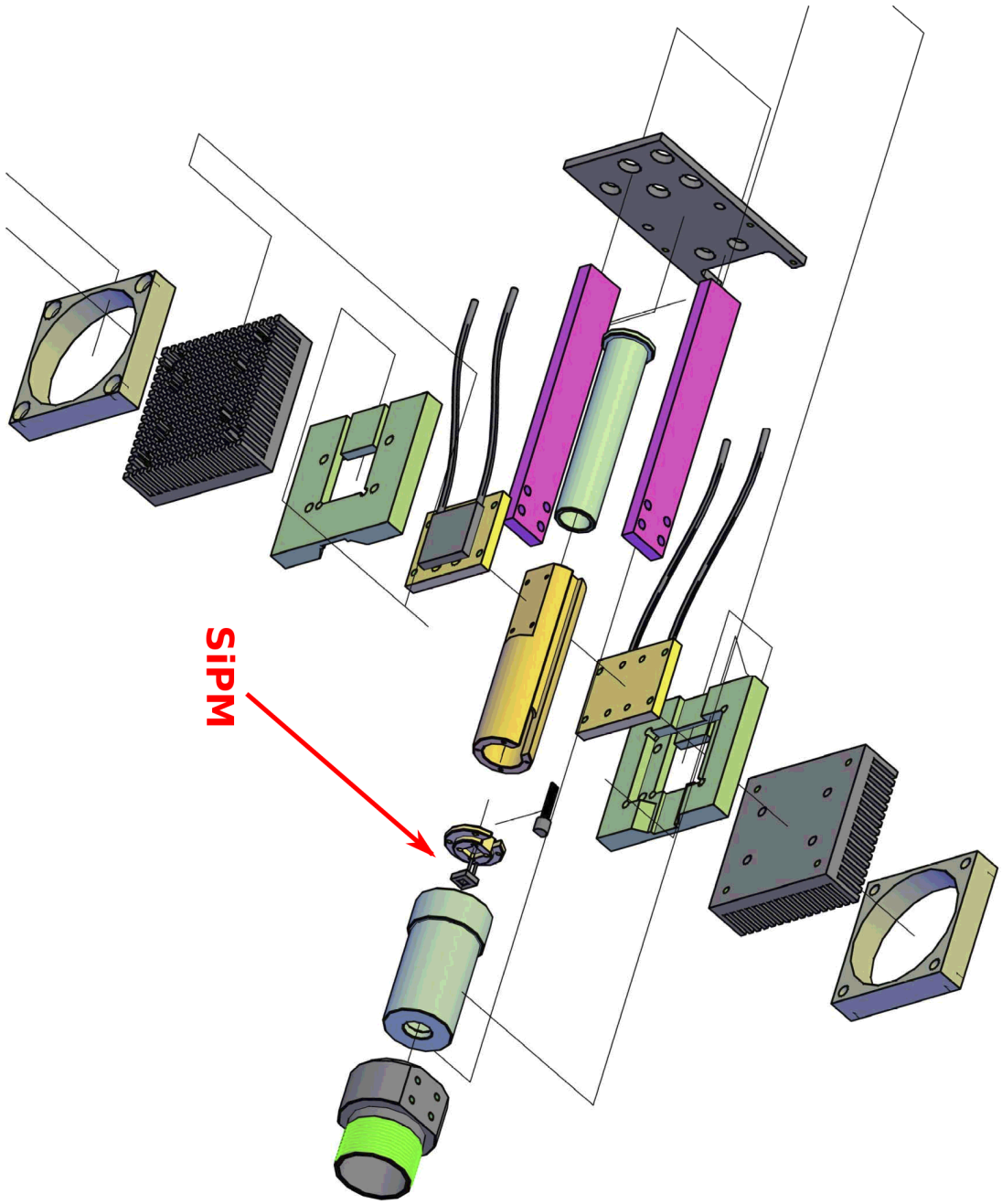

Figure C.1: Exploded drawing of the SiPM cooling mount. Image from [35]

D SiPM Preamplifier

Figure D.1: Schematic circuit of the amplifier board that fits inside the tube of the SiPM mount. Image from [36]

E Peltier Driver Circuit

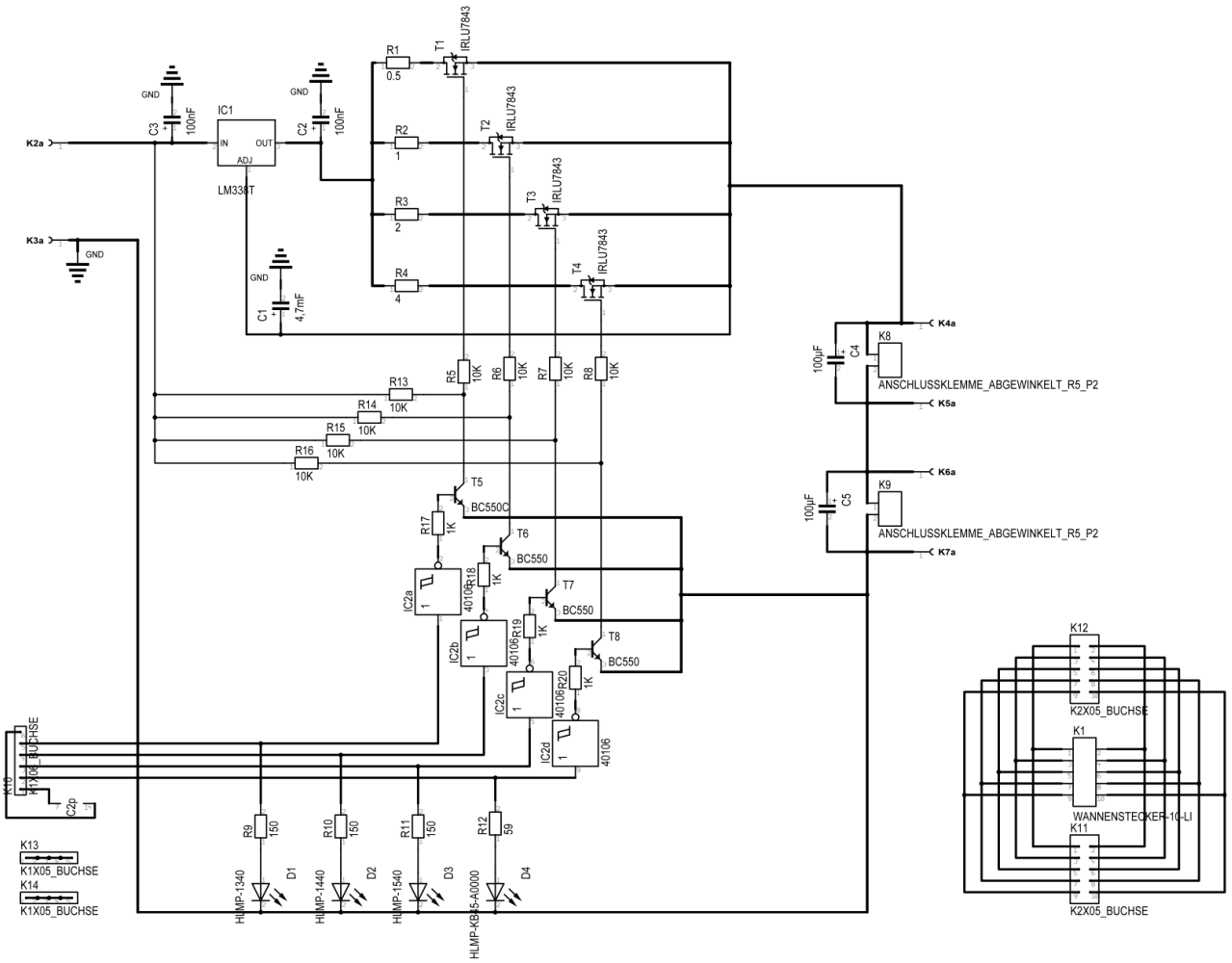

Figure E.1: Schematic circuit of the Peltier element controller board. Additionally, the headers for connecting the board with the backplane are shown.

Bibliography

[1] Benjamin Glauß. *Optical Test Stand and SiPM characteriation studies*. Master's Thesis, RWTH Aachen University, June 2012. Cited in 1.1, 2.6, 4.1, 4.1, 5.1.1.

[2] Johannes Schumacher. *Characterization Studies of Silicon Photomultipliers: Noise and Relative Photon Detection Efficiency*. Bachelor's Thesis, RWTH Aachen University, February 2011. Cited in 1.2, 2.2.2.

[3] H. Ibach and H. Lüth. *Festkörperphysik - Einführung in die Grundlagen*. Springer Verlag Berlin Heidelberg, 7th edition, 2009. Cited in 2.1.

[4] Dieter K. Schroder. *Semiconductor material and device characterization*. John Wiley & Sons, Ltd, 2006. Cited in 2.1.1.

[5] Gerhard Lutz. *Semiconductor Radiation Detectors*. Springer, 2nd printing of 1st edition, 2007. Cited in 2.1.1.

[6] S. M. Sze and Kwok K. Ng. *Physics of Semiconductor Devices*. Wiley Interscience, 3rd edition, 2007. Cited in 2.2, 2.3.

[7] R. Mirzoyan. Light emission in Si avalanches. *Nuclear Instruments and Methods in Physics Research A*, 610:98–100, May 2009. Cited in 2.1.1, 2.2.2, 2.12.

[8] William G. Oldham. Triggering phenomena in avalanche diodes. *IEEE*, 19(9): 1056–1060, 1972. Cited in 2.4.

[9] D. Renker and E. Lorenz. Advances in solid state photon detectors. *Journal of Instrumentation*, April 2009. Cited in 2.1.2, 2.1.2, 2.5, 2.2.1.

[10] Jörg Rennefeld. *Studien zur Eignung von Silizium Photomultipliern für den Einsatz im erweiterten CMS Detektor am SLHC*. Diploma Thesis, RWTH Aachen University, February 2010. Cited in 2.7.

[11] *MPPC Datasheet S10362-11 Series*. Hamamatsu, September 2012. Cited in 2.2.1, 2.8, 2.1.

[12] *MPPC Datasheet S10362-33 Series*. Hamamatsu, September 2012. Cited in 2.2.1, 2.1.

[13] *PM3350 Datasheet*. Ketek GmbH, September 2012. Cited in 2.2.1, 2.1.

[14] V. Andreev. A high-granularity scintillator calorimeter readout with silicon photomultipliers. *Nuclear Instruments and Methods in Physics Research A*, 540:368–380, March 2005. Cited in 2.9.

[15] S. Privitera et al. *Towards a new concept of photomultiplier based on silicon technology.* arxiv:0705.0672v1, May 2007. Cited in 2.2.2.

[16] R. Mirzoyan. The cross-talk problem in SiPMs and their use as light sensors for imaging atmospheric Cherenkov telescopes. *Nuclear Instruments and Methods in Physics Research A*, 610:131–134, May 2009. Cited in 2.2.2.

[17] Markus Lauscher. *Characterisation Studies of Silicon Photomultipliers for the Detection of Fluorescence Light from Extensive Air Showers.* Master's Thesis, RWTH Aachen University, January 2012. Cited in 2.2.2, 2.2.2, 2.2.2, 5.1.2, B.1.

[18] S. Cova et al. Evolution and prospects for single-photon avalanche diodes and quenching circuits. *Journal of Modern Optics*, 51:1267–1288, June 2004. Cited in 2.10, 2.11.

[19] Tim Niggemann. *New Telescope Design with Silicon Photomultipliers for Fluorescence Light Detection of Extensive Air Showers.* Master's Thesis, RWTH Aachen University, January 2012. Cited in 3.

[20] Geant 4 webpage. http://geant4.web.cern.ch, September 2012. Cited in 3.1.

[21] Florian Scheuch. *Measurements of a detector prototype with direct SiPM read-out and comparison with simulations.* Bachelor's Thesis, RWTH Aachen University, August 2010. Cited in 4.1.

[22] Simon Nieswand. *A Peltier cooling system for SiPM temperature stabilization.* Bacherlor's Thesis, RWTH Aachen University, October 2012. Cited in 4.2, 4.2.1, 4.3.

[23] *DS18B20 Programmable Resolution 1-Wire Digital Thermometer Datasheet.* Maxim Integrated, 2008. Cited in 4.2.1.

[24] *Digital-output relative humidity & temperature sensor/module datasheet.* Aosong(Guangzhou) Electronics Co.,Ltd, 2012. Cited in 4.2.1.

[25] Yu. G. Gurevich, G.N. Logvinov, O. Yu. Titov, and J. Giraldo. New physical principles of contact thermoelectric cooling. *Surface Review and Letters*, 9: 1703–1708, 2002. Cited in 4.4.

[26] *Peltier element datasheet.* QuickCool, October 2012. Cited in 4.2.1.

[27] *LM138, LM338 5-Amp Adjustable Regulators.* National Semiconductor, March 1995. Cited in 4.7.

[28] Arduino. Webpage of the arduino microcontroller boards. http://arduino.cc/playground/Code/PIDLibrary, September 2012. Cited in 4.2.2.

[29] Florian Scheuch. *Measurement and Simulation of Electrical Properties of SiPM Photon Detectors*. Master's Thesis, RWTH Aachen University, November 2012. Cited in 5.1.2.

[30] J. A. Hornbeck and J. R. Haynes. Trapping of Minority Carriers in Silicon. I. P-Type Silicon. *Physical Review*, 97:311 – 321, January 1954. Cited in 5.1.2.

[31] J. A. Hornbeck and J. R. Haynes. Trapping of Minority Carriers in Silicon. II. n-Type Silicon. *Physical Review*, 100:606–615, October 1955. Cited in 5.1.2.

[32] Marc Dejardin. Determination of the single pulse response of the cms-ecal electronics and application to the pulse shape reconstruction. *CMS Detector Note*, January 2008. Cited in 6.1.

[33] Tim Niggemann. Private communication, 2012. Cited in 6.4, 6.5.

[34] Markus Lauscher. Private communication, 2012. Cited in B.1.

[35] Barthel Philipps. Private communication, 2012. Cited in C.1.

[36] Franz Adamczyk. Private communication, 2012. Cited in D.1.

Acknowledgements

Ich bedanke mich bei Herrn Prof. Hebbeker, dass mir die Möglichkeit gegeben wurde an diesem Institut meine Masterarbeit anzufertigen. Auch danke ich Herrn Prof. Wiebusch, dass er sich bereit erklärt hat, die Zweitkorrektur zu übernehmen. Desweiteren danke ich Markus Merschmeyer für die unermüdliche Unterstützung bei der Anfertigung dieser Arbeit sowie für die Mühe beim Korrekturlesen. In diesem Zuge danke ich auch Carsten Heidemann für das Engagement das in die Korrektur meiner Arbeit geflossen ist. Großer Dank gilt auch Tim Niggemann der mich bei der Anwendung und Verbesserung der Simulation viel unterstützt hat. Danken möchte ich auch der Elektronikwerkstatt des III. Physikalischen Instituts A, insbesondere Franz Adamczyk für seine Hilfestellung bei der Entwicklung und Anfertigung der für diese Arbeit notwendigen Elektronik. Ebenfalls bedanke ich mich bei der Mechanikwerkstatt des III. Physikalischen Instituts A, an dieser Stelle besonders bei Barthel Philipps für die Unterstützung beim Entwurf und der Konstruktion der SiPM-Halterung. Ich möchte auch die zahlreichen Büro- und Flurnachbarn sowie die netten Institutskollegen nicht unerwähnt lassen mit denen eine gute Zusammenarbeit immer möglich war.
Dann danke ich auch meiner Familie ohne deren Unterstützung dieses Studium nicht möglich gewesen wäre sowie meiner Freundin, die mir während des Schreibens viel Arbeit Zuhause abgenommen hat.

Erklärung

Ich versichere, diese Arbeit selbstständig verfasst und keine anderen als die angegebenen Hilfsmittel und Quellen benutzt zu haben.
Aachen, November 2012

Andreas Künsken